

The GALAH survey: Milky Way disc metallicity and alpha-abundance trends in combined APOGEE-GALAH catalogues

Govind Nandakumar^{1,2*}, Michael R. Hayden^{3,2}, Sanjib Sharma^{3,2}, Sven Buder^{1,2}, Martin Asplund⁴, Joss Bland-Hawthorn^{3,2}, Gayandhi M. De Silva^{5,6}, Valentina D’Orazi⁷, Ken C. Freeman¹, Janez Kos⁸, Geraint F. Lewis³, Sarah L. Martell^{9,2}, Katharine J. Schlesinger¹, Jane Lin^{1,2}, Jeffrey D. Simpson^{9,2}, Daniel B. Zucker^{10,6}, Tomaž Zwitter⁸, Thomas Nordlander^{1,2}, Luca Casagrande^{1,2}, Karin Lind¹¹, Klemen Côtar⁸, Dennis Stello¹⁰, Robert A. Wittenmyer¹² and Thor Tepper-Garcia^{3,2,13}

¹Research School of Astronomy & Astrophysics, Australian National University, ACT 2611, Australia

²Centre of Excellence for Astrophysics in Three Dimensions (ASTRO-3D), Australia

³Sydney Institute for Astronomy, School of Physics, A28, The University of Sydney, NSW 2006, Australia

⁴Max Planck Institute for Astrophysics, Karl-Schwarzschild-Str. 1, D-85741 Garching, Germany

⁵Australian Astronomical Optics, Faculty of Science and Engineering, Macquarie University, Macquarie Park, NSW 2113, Australia

⁶Macquarie University Research Centre for Astronomy, Astrophysics & Astrophotonics, Sydney, NSW 2109, Australia

⁷Istituto Nazionale di Astrofisica, Osservatorio Astronomico di Padova, vicolo dell’Osservatorio 5, 35122, Padova, Italy

⁸Faculty of Mathematics and Physics, University of Ljubljana, Jadranska 19, 1000 Ljubljana, Slovenia

⁹School of Physics, UNSW, Sydney, NSW 2052, Australia

¹⁰Department of Physics and Astronomy, Macquarie University, Sydney, NSW 2109, Australia

¹¹Department of Astronomy, Stockholm University, AlbaNova University Center, SE-106 91 Stockholm - Sweden

¹²University of Southern Queensland, Centre for Astrophysics, USQ Toowoomba, QLD 4350 Australia

¹³Centre for Integrated Sustainability Analysis, The University of Sydney, 2006, Australia

Accepted XXX. Received YYY; in original form ZZZ

ABSTRACT

GALAH and APOGEE are two high resolution multi object spectroscopic surveys that provide fundamental stellar parameters and multiple elemental abundance estimates for > 400,000 stars in the Milky Way. They are complimentary in both sky coverage and wavelength regime. Thus combining the two surveys will provide us a large sample to investigate the disc metallicity and alpha abundance trends. We use the *Cannon* data-driven approach selecting training sets from among ~20,000 stars in common for the two surveys to predict the GALAH scaled stellar parameters from APOGEE spectra as well as APOGEE scaled stellar parameters from GALAH spectra. We provide two combined catalogues with GALAH scaled and APOGEE scaled stellar parameters each having ~500,000 stars after quality cuts. With ~470,000 stars that are common in both these catalogues, we compare the GALAH scaled and APOGEE scaled metallicity distribution functions (MDF), radial and vertical metallicity gradients as well as the variation of $[\alpha/\text{Fe}]$ vs $[\text{Fe}/\text{H}]$ trends along and away from the Galactic mid plane. We find mean metallicities of APOGEE scaled sample to be higher compared to that for the GALAH scaled sample. We find similar $[\alpha/\text{Fe}]$ vs $[\text{Fe}/\text{H}]$ trends using both samples consistent with previous observational as well as simulation based studies. Radial and vertical metallicity gradients derived using the two survey scaled samples are consistent except in the inner and outer Galactocentric radius bins. Our gradient estimates in the solar neighborhood are also consistent with previous studies and are backed by larger sample size compared to previous works.

Key words: Galaxy: disc - Galaxy: evolution - Galaxy: formation - Galaxy: structure - stars: abundances - surveys

1 INTRODUCTION

The field of Galactic archaeology (Freeman & Bland-Hawthorn 2002) deals with dissecting the Milky Way into its various components with the aim to unravel the processes that contributed to the formation and evolution of our Galaxy. We rely on observation of

stars, gas and dust in the Galaxy using a broad range of the electromagnetic spectrum to achieve this goal.

There are a plethora of data available in the form of spectra, astrometric and photometric information as well as multi wavelength maps with the advent of large scale spectroscopic (Apache Point Observatory Galactic Evolution Experiment/APOGEE: Eisenstein et al. 2011, RAdial Velocity Experiment/RAVE: Steinmetz et al. 2006, Gaia-ESO: Gilmore et al. 2012, Large Sky Area Multi-Object Fiber Spectroscopic Telescope/LAMOST: Cui et al. 2012, Galactic

* E-mail: govind.nandakumar@anu.edu.au

Archaeology with HERMES/GALAH: De Silva et al. 2015, Abundances and Radial velocity Galactic Origins Survey/ARGOS: Ness et al. 2012), astrometric (Hipparcos: Perryman et al. 1997, *Gaia*: Gaia Collaboration et al. 2016) and photometric surveys (Two-Micron All Sky Survey/2MASS: Skrutskie et al. 2006, Sloan Digital Sky Survey/SDSS: Stoughton et al. 2002, Vista Variables in the Vía Láctea/VVV: Minniti et al. 2010, the SkyMapper Southern Survey : Wolf et al. 2018). From being limited to the solar neighborhood a decade ago, our understanding of the Milky Way and its components has thus extended to as far as the Galactic centre, outer Galaxy including the halo with the improved chemodynamic information of stellar populations from these surveys. For e.g., star count observations in the solar neighborhood (Yoshii 1982; Gilmore & Reid 1983) led to the discovery of the thick disc, followed by its characterisation as the old α -enhanced population in the double sequence exhibited by the solar neighborhood stars in the $[\alpha/\text{Fe}]$ vs $[\text{Fe}/\text{H}]$ plane (Fuhrmann 1998; Bensby et al. 2003; Reddy et al. 2006; Adibekyan et al. 2012; Haywood et al. 2013). At present data from large scale spectroscopic surveys (Anders et al. 2014; Hayden et al. 2015; Weinberg et al. 2019) have led to the exploration of this trend at different galactocentric radius, R , and average height, $|Z|$, across the Galaxy shedding light on the disc formation and evolution scenarios. Add to that the recent advent in the accurate age determination methods thus providing valuable information about the star formation histories and age metallicity relation of disc stellar populations (Casagrande et al. 2011; Bedell et al. 2018; Lin et al. 2020; Nissen et al. 2020). Various secular processes such as radial migration (Sellwood & Binney 2002; Schönrich & Binney 2009; Minchev & Famaey 2010), that are among the suggested mechanisms leading to the mixing of stars across the Galaxy, are also being explored using a combination of accurate phase space information from *Gaia* (Gaia Collaboration et al. 2018) and chemistry and age information of stars across the Galaxy from large scale spectroscopic surveys (Buder et al. 2019). The discovery of streams and dynamically different stellar populations in the Milky Way halo, considered to be the result of past accretion/merger events (Belokurov et al. 2018; Helmi et al. 2018; Ibata et al. 2019; Myeong et al. 2019) using the *Gaia* data and their further exploration with chemistry from large scale spectroscopic surveys (Buder et al. in prep) is another example. Many spectroscopic surveys have also been able to observe a statistically significant number of stars located in the Milky Way Bulge that led to the discovery of multiple components in the Bulge metallicity distribution function (MDF). These components are now being studied in detail to understand the origin of the Bulge and its connection with the Milky Way bar and Galaxy evolution (Ness et al. 2013; Rojas-Arriagada et al. 2017, 2020). There are many upcoming surveys (4-metre Multi-Object Spectroscopic Telescope/4MOST : de Jong et al. (2019), Sloan Digital Sky Survey/SDSS-V : Kollmeier et al. (2017), WEAVE : Dalton et al. (2018)) that will further our understanding of the formation and evolution of the Milky Way and its components.

Using data from such large scale spectroscopic surveys, various disc formation and evolution scenarios are being explored by studying the disc metallicity and alpha abundance trends. For e.g., formation of the thick disc via a violent merger of a smaller satellite onto a pre-existing disc with vertical chemical gradients (Quinn et al. 1993) can lead to heating the least bound disc stars (that are metal poor and old) into large scale heights, and thus result in a negative vertical metallicity gradient. Radial migration due to mergers and/or early encounters (Quillen et al. 2009; Bird et al. 2012) or internal processes like scattering by transient spiral structure (Sellwood & Binney 2002) or bar-spiral resonances overlap (Minchev & Famaey 2010; Brunetti et al. 2011) in a disc formed inside out can lead to

flattening of radial metallicity gradient with height from the plane (as shown in MinchevMinchev: et al. 2014). Meanwhile, thick disc formation by stellar accretion from small satellite mergers (Abadi et al. 2003) or accretion of gas rich materials at high redshifts (Brook et al. 2004, 2005; Bournaud et al. 2009) are found to produce no vertical metallicity gradients. Thus mean metallicity variation of disc stellar populations with R , $|Z|$ (Hayden et al. 2015; Schlesinger et al. 2014) as well as radial and vertical metallicity gradients (Hartkopf & Yoss 1982; Chen et al. 2003; Yong et al. 2006; Kordopatis et al. 2011; Mikolaitis et al. 2014; Bergemann et al. 2014; Cunha et al. 2016; Duong et al. 2018, Spina et al. submitted etc.) found using data from spectroscopic surveys are strong signatures of certain proposed disc formation and evolution scenarios. For a reliable comparison of observed chemical trends with those from simulations and models, we need unbiased and spatially extended set of stars covering the Milky Way disc along and away from the Galactic mid plane.

The above mentioned large scale spectroscopic surveys derive fundamental stellar parameters and elemental abundances from observed stellar spectra via dedicated pipelines using spectral fitting routines that fit observed spectra with synthetic spectra generated from stellar model atmospheres, model grids and linelists, all of which are different/specific to the respective survey. Thus, even though there are overlaps in the observed stars between many spectroscopic surveys, there are significant systematic differences in their derived stellar parameters as well as abundances. This difference can also lead to misinterpretation of abundance trends estimated using the derived parameters from different surveys. Thus it is necessary to combine such complementary surveys with their parameters scaled with respect to either survey so that the resulting volume complete sample can be used to map and decipher the global chemodynamic trends of stellar populations in the Milky Way.

One step toward this direction of combining surveys (or scaling them with respect to each other) was made with the introduction of the data driven approach known as the *Cannon* (Ness et al. 2015). Ho et al. (2017) used the *Cannon* to derive the stellar parameters for around 4,50,000 giant stars in LAMOST (low spectral resolution survey) by bringing them to the scale of APOGEE (high spectral resolution) survey. Recently, Wheeler et al. (2020) used the *Cannon* to estimate abundances representing five different nucleosynthetic channels, for 3.9 million stars in LAMOST, by training LAMOST spectra with GALAH DR2 stellar parameters and abundances (also referred to as "labels") for stars in common to both surveys. The *Cannon* has also been used to propagate information from one survey to another, and to derive higher precision stellar parameters, abundances, mass and age information using survey pipeline estimate as the training set labels (Ness et al. 2016; Casey et al. 2017; Buder et al. 2018; Zhang et al. 2019; Hasselquist et al. 2020 etc.). The *Starnet* (Fabbro et al. 2018), a convolutional neural network model, was able to predict stellar parameters by training on APOGEE spectra with APOGEE Stellar Parameter and Chemical Abundance Pipeline (ASPCAP) labels (T_{eff} , $\log g$ and $[\text{Fe}/\text{H}]$). When compared with the *Cannon* results trained on the same data, the *Starnet* showed similar behaviour, though the *Starnet* performs poorly on small training sets compared to the *Cannon*. A deep neural network designed by Leung & Bovy (2019) was used to determine stellar parameters from APOGEE spectra using the full wavelength range, while censored portions of the spectrum were used to derive individual element abundances. The *Payne* (Ting et al. 2019) is another tool that explicitly models spectra as a function of stellar parameters. Xiang et al. (2019) used the data driven *Payne* to train a model that predicts stellar parameters and abundances for 16 elements from LAMOST DR5 spectra using stars in common with APOGEE DR14 and GALAH

DR2 as the training set. Thus there are many tools and methods available to put different surveys on the same scale.

In this work, we use the data driven approach, the *Cannon* 2 (Ness et al. 2015; Casey et al. 2016), to put the stellar parameters (T_{eff} , $\log g$ and $[\text{Fe}/\text{H}]$) and general $[\alpha/\text{Fe}]$ abundance on the same scale for the surveys, APOGEE and GALAH. For this, we have to select a training set composed of common stars observed in both the surveys, with high fidelity stellar labels as well as high quality spectra. Since both the surveys yield stellar parameters and abundances with dedicated pipelines from high resolution spectra (though in different wavelength ranges), we cannot choose either survey to be the best. Hence, we carry out the exercise in both ways, i.e., (i) train *Cannon* model on APOGEE spectra with GALAH labels and (ii) train *Cannon* model on GALAH spectra with APOGEE labels and derive stellar parameters and $[\alpha/\text{Fe}]$ values for both cases. We also use the *Cannon* to (iii) train *Cannon* model on GALAH spectra with GALAH labels and (iv) *Cannon* model on APOGEE spectra with APOGEE labels, so that we can combine (i) and (iii) to provide the GALAH scaled stellar parameter catalogue, and (ii) and (iv) to provide the APOGEE scaled stellar parameter catalogue. We use the common stars in these catalogues to compare the metallicity and $[\alpha/\text{Fe}]$ distribution functions, $[\alpha/\text{Fe}]$ vs $[\text{Fe}/\text{H}]$ trends, radial and vertical metallicity gradients at different R and $|Z|$ locations across the Galaxy between the two surveys as well as with other previous studies.

We describe the data used in this paper in Section 2. In Section 3, we give a brief description of the *Cannon*, followed by the training set selection for APOGEE-GALAH (APOGEE spectra trained with GALAH labels) and GALAH-APOGEE (GALAH spectra with APOGEE labels) and finally the cross validation using the *Cannon* prediction for each training set. We discuss the *Cannon* results and their limitations from all APOGEE and GALAH spectra in Section 4, and compare the MDF, $[\alpha/\text{Fe}]$ trends, radial and vertical metallicity gradients at different R and $|Z|$ locations across the Galaxy with the *Cannon* results. We summarise our results and discuss future works in Section 5.

2 DATA

Here we describe the data used in this work. We use the latest available data release of APOGEE (DR16) and GALAH (DR3). We make use of the fundamental stellar parameters : T_{eff} , $\log g$, $[\text{Fe}/\text{H}]$ and $[\alpha/\text{Fe}]$ from those catalogues, and use the star spectra that are provided along with them.

2.1 APOGEE

Started as one of the four programs in the Sloan Digital Sky Survey III (SDSS-III; Eisenstein et al. 2011), the Apache Point Observatory Galaxy Evolution Experiment (APOGEE, Majewski et al. 2017) continues as part of SDSS-IV (Blanton et al. 2017) observing in the near-infrared H-band (1.5–1.7 μm) at high spectral resolution ($R \sim 22,500$) and high signal-to-noise ratios, S/N, in the Northern and Southern hemispheres. While the APOGEE survey makes use of the Sloan 2.5 m Telescope (Gunn et al. 2006) at the Apache Point Observatory (APO) in the Northern hemisphere, the APOGEE-2 survey collects data using the 2.5m du Pont telescope at Las Campanas Observatory (LCO; Bowen & Vaughan 1973) with the twin Near infrared (NIR) spectrograph (Wilson et al. 2019).

We make use of the data products from the latest data release, DR16 (Ahumada et al. 2019), which contains a total of 473,307 sources with derived atmospheric parameters and abundances from

the APOGEE Stellar Parameters and Chemical Abundances Pipeline (ASPCAP; García Pérez et al. 2016). For our work, we use the calibrated "PARAM" stellar parameters and abundances described in Jönsson et al. (2020). In addition to the catalogue, we also make use of the "apStar" and "asStar" spectra¹ which are the combined spectra of multiple visits, all in a common rest frame and identical wavelength solution across all sources.

2.2 GALAH

Galactic Archaeology with HERMES (GALAH; De Silva et al. 2015) is a high resolution spectroscopic survey of the Milky Way using the High Efficiency and Resolution Multi-Element Spectrograph (HERMES; Barden et al. 2010; Sheinis et al. 2015) on the Anglo-Australian Telescope. The HERMES spectrograph provides high-resolution ($R \sim 28,000$) spectra of up to 392 objects in four wavelength bands: 4713-4903Å (blue arm), 5648-5873Å (green arm), 6478-6737Å (red arm), and 7585-7887Å (infrared arm). The latest GALAH data release (GALAH DR3; Buder & The GALAH Team 2020), which includes the K2-HERMES survey (Wittenmyer et al. 2018; Sharma et al. 2019) and the TESS-HERMES survey (Sharma et al. 2018), provides up to 30 element abundances of various nucleosynthesis channels for 588,571 stars, and publish 678,423 spectra including repeat observations. Here we will refer to them collectively as the GALAH survey. In this data release, all stellar parameters and elemental abundances have been estimated via the spectrum synthesis code Spectroscopy Made Easy (SME; Valenti & Piskunov 1996; Piskunov & Valenti 2017) with 1D MARCS stellar atmosphere models (Gustafsson et al. 2008). In addition, non-LTE computations have been used for 11 elements (Li, C, O, Na, Mg, Al, Si, K, Ca, Mn, Fe and Ba) to estimate their elemental abundances Amarsi et al. (2020).

3 METHOD

3.1 The Cannon

The *Cannon* (Ness et al. 2015), in simple terms, is a data driven method which generates a model for stellar spectra based on a training set of spectra, for which the stellar parameters and abundances are known with high fidelity (i.e. high SNR and/or accurate estimates). This model can then be used to infer the same labels for any set of continuum normalised spectra that have been sampled onto a common wavelength grid with uniform start and end wavelengths as that of the training set. The *Cannon* relies on the following assumptions: similar labels imply similar spectra and each spectrum is a smooth function of its labels such that changes in labels result in a smooth variation of spectra.

In the training step, the spectral model coefficients are fit at each wavelength pixel while keeping the labels fixed for all training set star spectra. The spectral model thus generated characterises the flux at each wavelength pixel as a function of the given labels, with label coefficient values describing the influence of the corresponding label at a certain wavelength pixel. In the test step, the label coefficients are fixed, while likelihood optimization is carried out to predict the labels from the flux values at each wavelength pixel of each test spectrum.

We use the *Cannon* 2 described in Casey et al. (2016)² and use a quadratic model with T_{eff} , $\log g$, $[\text{Fe}/\text{H}]$, $[\alpha/\text{Fe}]$, microturbulence

¹ <https://data.sdss.org/sas/dr16/apogee/spectro/redux/r12/stars/>

² <https://github.com/andy-casey/AnniesLasso>

APOGEE [DR16] - GALAH SME [DR3] (5739)

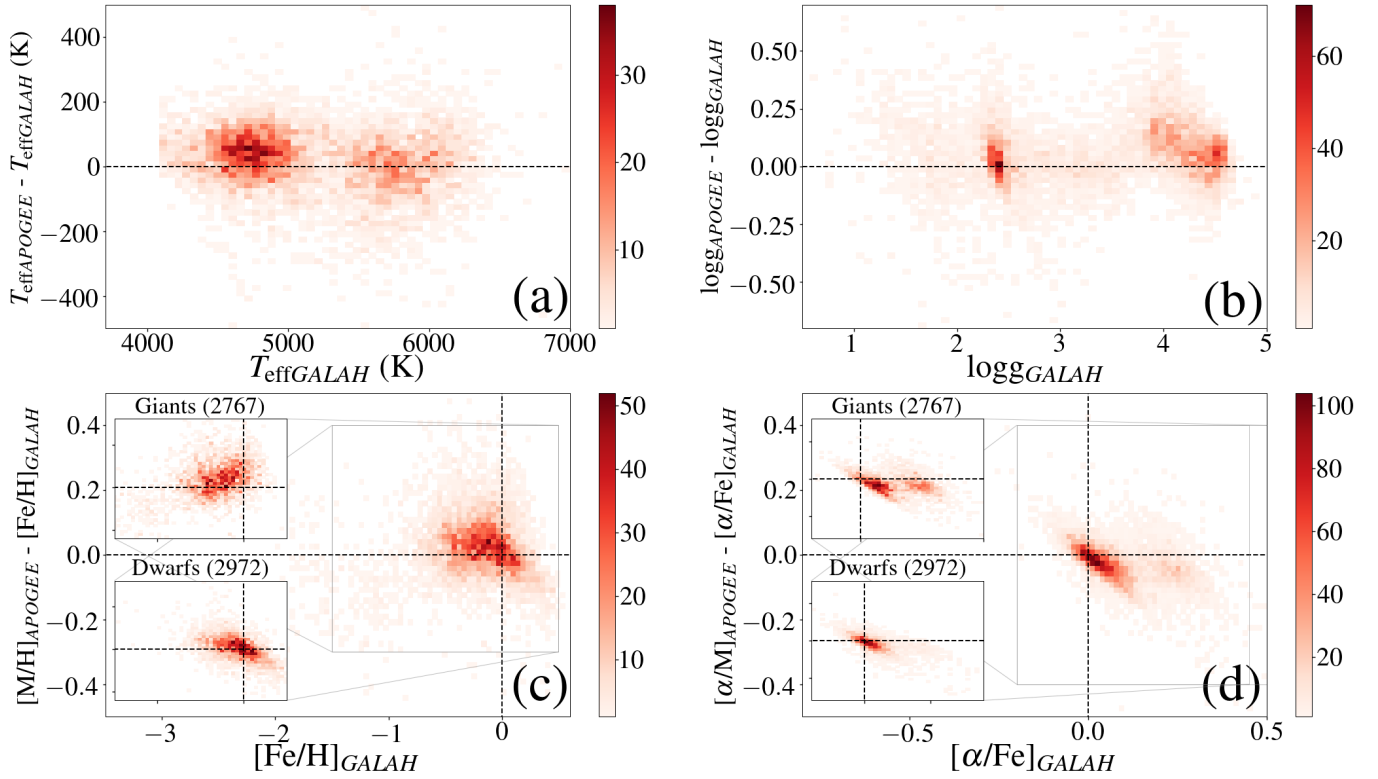


Figure 1. The difference in derived stellar parameters as a function of GALAH SME values (APOGEE - GALAH vs GALAH) for 5739 stars (shown as 2d histogram colour coded by the number of stars in each bin) in the high fidelity training set used to train APOGEE spectra with GALAH SME stellar parameters. (a) T_{eff} , APOGEE ASPCAP values are higher by a median value of 100 - 150 K for 4000-5200 K GALAH SME derived range and the difference gradually decreases for hotter stars. There is a large dispersion that ranges from -500 K to + 500 K across the full T_{eff} range. (b) $\log g$, difference values vary from -0.6 dex to +0.6 dex, with red clump stars in both surveys having similarly determined values and the APOGEE ASPCAP values for dwarfs being higher than that determined by GALAH. (c) $[\text{Fe}/\text{H}]$, the difference trend shows APOGEE metallicities to be lower than GALAH for metal poor GALAH stars ($[\text{Fe}/\text{H}] < \sim -0.8$ dex), higher for sub solar GALAH metallicities and finally slightly lower again for super solar GALAH metallicities. In the insets, we show the difference trend for giants and dwarfs separately, which indicates that the metallicity difference changes from lower to higher in a linear fashion for giants and vice versa for dwarfs. (d) $[\alpha/\text{Fe}]$, both surveys exhibit a bimodal $[\alpha/\text{Fe}]$ distribution, with APOGEE values slightly higher for subsolar α stars in GALAH and lower for super solar α stars in GALAH. The difference trends for giants and dwarfs are shown in separate insets, where we find giants have significant numbers in both high and low α regimes, while dwarfs are concentrated more in the low α regime, with similar trend exhibited by both populations.

(v_{micro}), and line broadening (v_{broad}) as the labels, resulting in a spectral model of the following form :

$$F_{n\lambda} = v(l_n) \cdot \theta_\lambda + \text{noise} \quad (1)$$

where $F_{n\lambda}$ is the flux at each wavelength pixel, λ , for each star, n , in the training set. θ_λ is the set of spectral model coefficients for multiple label combinations at each λ , l_n represents the labels and $v(l_n)$ is the "vectorizing function", which is in the form of a 2 degree quadratic polynomial and the labels have been normalised or scaled in the following manner:

$$\hat{l}_n = \frac{l_n - l_{n,50}}{l_{n,97.5} - l_{n,2.5}} \quad (2)$$

The next step is to choose a high quality training set that can be used to generate the required *Cannon* spectral model as described above.

3.2 Training set

We select the stars in common between both APOGEE and GALAH as the basic training set. We find 17,721 stars based on cross match using the *APOGEE_ID* and *star_id* columns in APOGEE DR16 and GALAH DR3 catalogues with *Topcat* (Taylor 2005, 2020). Because both APOGEE and GALAH observe multiple spectra for several stars, both *APOGEE_ID* and *star_id* are not unique. GALAH has a unique identifier, *subject_id*, that can be used to identify the spectra of the same star that has been observed at different epochs, in the cross match set. We combined the *APOGEE_ID* and *LOCATION_ID* to create a unique id for APOGEE as well (APOGEE_UniqueID) that allows the identification of repeated spectra in the cross match. In the following subsections, we go into the details in the selection of training sets for APOGEE-GALAH and GALAH-APOGEE.

GALAH SME [DR3] - APOGEE [DR16] (6817)

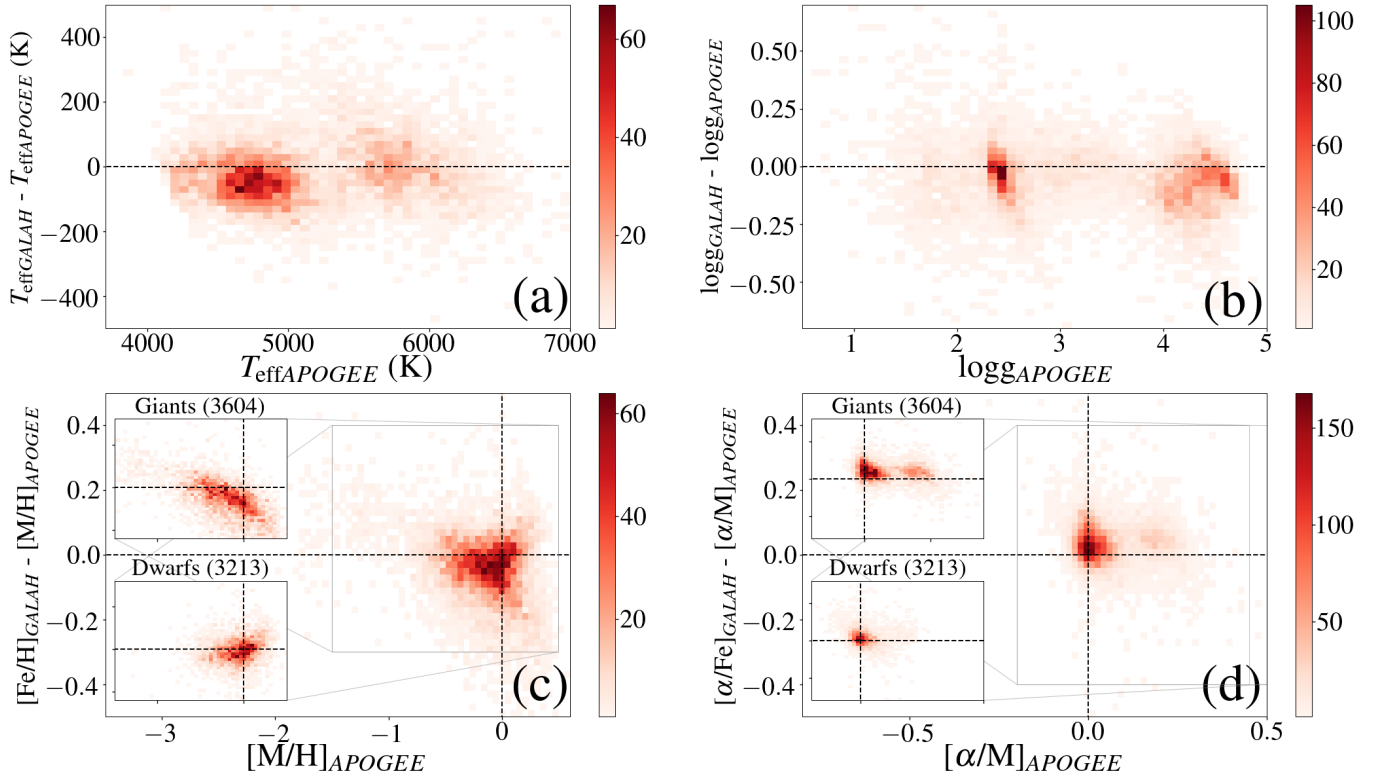


Figure 2. The difference in derived stellar parameters as a function of APOGEE ASPCAP values (GALAH - APOGEE vs APOGEE) for 6817 stars (shown as 2d histogram colour coded by the number of stars in each bin) in the high fidelity training set used to train GALAH spectra with APOGEE ASPCAP stellar parameters. The trends we see here are in fact the inverse of those in Figure 1 since we invert the y-axis, but here the x-axis values are different. (a) T_{eff} and (b) $\log g$ are the inverse trend of Figure 1 (a) and (b). (c) $[\text{Fe}/\text{H}]$, there is a bifurcation in the difference trend in super solar APOGEE metallicity regime, which can be seen as the difference in the trends of giants and dwarfs shown in insets. (d) $[\alpha/\text{Fe}]$, APOGEE values exhibit dispersion and are consistently lower compared to GALAH in the entire $[\alpha/\text{M}]$ range. The trends for giants and dwarfs are shown in separate insets.

3.2.1 Training set for APOGEE-GALAH

Here we describe the selection of the training set used to train APOGEE spectra with GALAH labels. Among 17,721 stars in the cross match, there are multiple GALAH parameters (from separate GALAH observations at different epochs of the same star) for the same APOGEE spectrum. In such cases, we choose the GALAH parameters corresponding to the lowest chi-square value from the SME fit (chi2_sp). At the same time, there are multiple APOGEE spectra (identified by the APOGEE_UniqueID) for which GALAH parameters are fixed (since there is only one GALAH observation/spectrum). We make sure these remain in the catalogue. This leads to a catalogue of 12,041 stars. Next, we remove stars with invalid GALAH and APOGEE parameters in our label space, and further select high reliable and high quality GALAH labels/stellar parameters by the following constraints :

$$\text{snr_c2_iraf} > 25 \quad \text{flag_sp} = 0 \quad \text{chi2_sp} < 4 \quad (3)$$

where snr_c2_iraf is the signal-to-noise ratio (SNR) of spectra in the green arm (chip 2) and flag parameter, flag_sp , describes various GALAH reduction and analysis issues indicating the quality of spectra and estimated stellar parameters.

In addition, we select good quality APOGEE spectra with $\text{SNR} >$

80 and neglecting spectra with *STARFLAG*³ bits set for selected few bits (0: bad pixels, 3: very bright neighbor, 4: low snr, 9: significant number of pixels in high persistence region, 10: significant number of pixels in medium persistence region, 11: significant number of pixels in low persistence region, 12: obvious positive jump in blue chip, 13: obvious negative jump in blue chip and 17: Broad lines).

After these cuts, there are 5739 stars in the high fidelity training set. In Fig 1, we show the systematic difference in T_{eff} (Fig 1a), $\log g$ (Fig 1b), $[\text{Fe}/\text{H}]$ (Fig 1c) and $[\alpha/\text{Fe}]$ (Fig 1d) for these stars, with APOGEE on the x axis and APOGEE-GALAH on the y axis. It is clear that APOGEE derived values are slightly higher compared to GALAH for the majority of stars in the case of T_{eff} , $\log g$ and $[\text{Fe}/\text{H}]$, while there is a large scatter. The difference in T_{eff} has a root mean square value of 102 K, $\log g$: 0.15 dex, $[\text{Fe}/\text{H}]$: 0.16 dex and $[\alpha/\text{Fe}]$: 0.07 dex. We find a trend in the difference of $[\alpha/\text{Fe}]$ to vary from positive to negative for low $[\alpha/\text{Fe}]_{\text{GALAH}}$ (-0.2 dex to 0.15 dex) with a negative slope, while the trend is flatter varying from nearly zero to negative for high $[\alpha/\text{Fe}]_{\text{GALAH}}$ (0.15 dex to 0.4 dex). In the case of metallicities, we find APOGEE ASPCAP metallicities to be higher in the sub solar GALAH metallicity regime, gradually changing to

³ https://www.sdss.org/dr14/algorithms/bitmasks/#APOGEE_STARFLAG

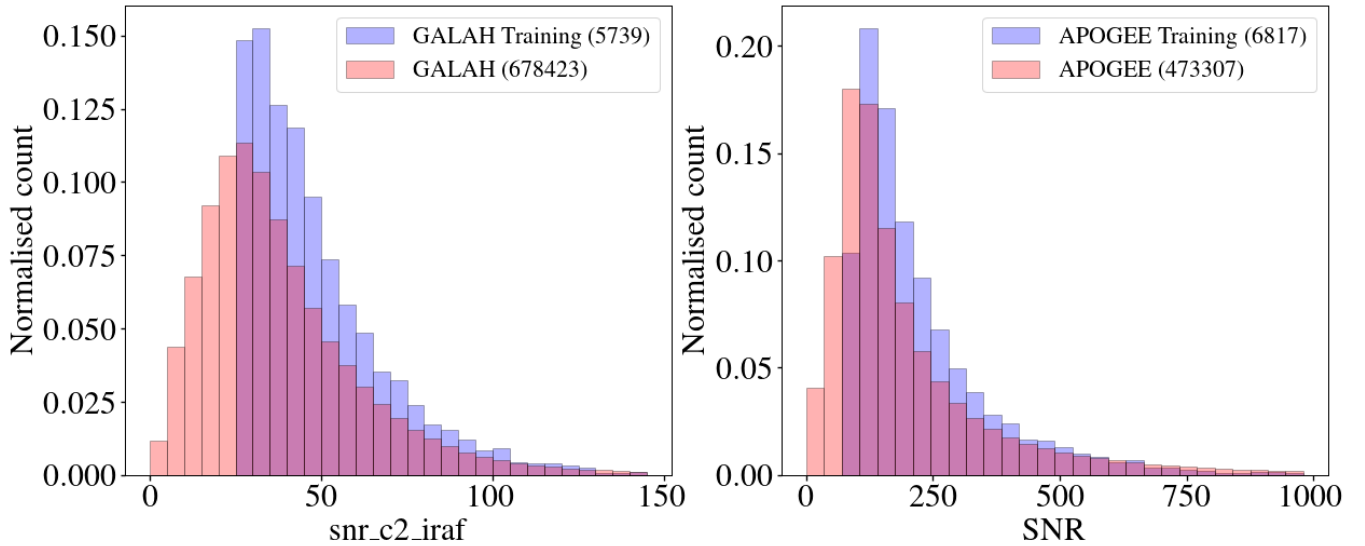


Figure 3. Comparison of the signal-to-noise ratio (SNR) distribution of training set stars (blue) and all stars (red) for GALAH (left panel) and APOGEE (right panel) surveys. It is clear that GALAH spectra has 4 times lower SNR compared to APOGEE and our chosen training set spectra have SNRs higher than 50th percentile value of the whole distributions.

being lower in the super solar GALAH metallicity regime compared to that derived by GALAH SME. When we split the sample into giants ($\log g_{GALAH} < 3.5$) and dwarfs ($\log g_{GALAH} > 3.5$), we find the trend to vary from negative to positive as we move from metal poor to metal rich regime for giants (top inset in Fig. 1c). We find a completely different trend for dwarfs (bottom inset in Fig. 1c), with APOGEE ASPCAP metallicities being higher for metal poor GALAH stars (< -0.5 dex) but lower with increasing GALAH metallicity. Similar inset plots for giants and dwarfs in the case of $[\alpha/Fe]$ are shown in Fig. 1d, where dwarfs are concentrated close to the solar regime and APOGEE $[\alpha/M]$ values vary from higher to lower in the sub solar to super solar $[\alpha/Fe]_{GALAH}$ regime with a negative slope, indicating a broader distribution of GALAH $[\alpha/Fe]$ values compared to APOGEE. We find giants exhibiting a stronger bimodal $[\alpha/Fe]$ distribution while being concentrated more in the super solar GALAH $[\alpha/Fe]$ regime. The majority of APOGEE $[\alpha/M]$ values are lower compared to that derived by GALAH in this regime. Overall, we find APOGEE metallicities to be higher and exhibiting lower dispersion $[\alpha/Fe]$ values compared to GALAH.

3.2.2 Training set for GALAH-APOGEE

Similar to 3.2.1, here we describe the training set selection to train GALAH spectra with APOGEE labels. We follow the same procedure by checking for the same GALAH spectrum for which there are different APOGEE ASPCAP stellar parameters (from separate observations at different epochs of the same star). In such cases, we select the APOGEE parameters for spectra with the highest SNR. As in 3.2.1, we keep the stars with different GALAH spectra for which there is only one APOGEE observation/spectrum and hence only one set of stellar parameters. There are 10,080 stars remaining in the catalogue after these procedures. We remove stars with invalid APOGEE and GALAH parameters (-9999.0 or NULL value) and further select high fidelity stars by following constraints in SNR :

$$snr_c2_iraf > 25 \quad SNR > 80 \quad (4)$$

In addition, we remove stars for which selected bits (16: bad T_{eff} ,

17: bad $\log g$, 18: bad v_{micro} , 19: bad metals, 20: bad $[\alpha/Fe]$ and 23: bad overall for star) in the ASPCAPFLAG⁴ has been set. We removed GALAH spectra with no chip4 data, that were observed during December 2018 (identified by subject_id starting with 1812). We also identified certain GALAH star spectra with bad normalization for chip 4 (identified by subject_ids starting with : 1407080012, 1407080041, 1407080071, 1512270042 and 1512270052). After implementing all of the above mentioned cuts, there are 6817 stars in the final training set.

In Fig 2, we show the difference in derived stellar parameters (GALAH - APOGEE vs APOGEE) for 6817 stars in the high fidelity training set used to train GALAH spectra with APOGEE ASPCAP stellar parameters. This is basically the inversion of the Y-axis and change of the X-axis (from GALAH to APOGEE) shown in the Fig 1 and hence we see the trends to be inverted, though the numbers are different due to the difference in training set selection methods for APOGEE-GALAH and GALAH-APOGEE described above. There is bifurcation of the metallicity difference trend for APOGEE stars with super solar metallicities, which can be seen as the effect of the stellar population to which they belong, i.e., APOGEE giants/dwarfs have higher/lower metallicity than GALAH. This was also seen in Fig 1 c as the clump of stars in the GALAH metallicity range of -0.5 to 0.0 dex for which APOGEE metallicities are higher by $\sim 0.1-0.2$ dex and belong to giants. Meanwhile, GALAH dwarfs have only slightly higher metallicity compared to that of APOGEE in the super solar GALAH metallicity regime in Fig 1 c, which makes sure that they still lie in the super solar metallicity regime in the case of APOGEE and thus we see a bifurcation. In the case of $[\alpha/Fe]$, the majority of APOGEE stars have slightly higher values and have narrower distributions compared to GALAH.

⁴ <https://www.sdss.org/dr14/algorithms/bitmasks/>

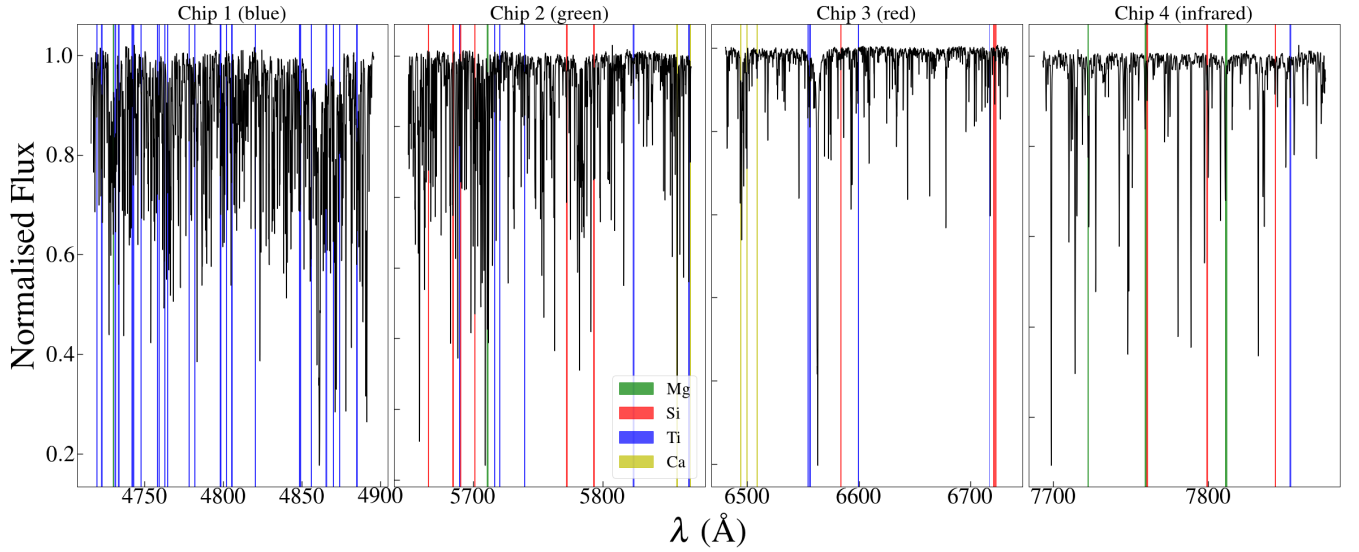


Figure 4. An example of GALAH spectra (black) covering the wavelength range from ~ 4725 to ~ 7900 Å in 4 chips (blue, green, red and infra red) with gaps in between. Different colours indicate the masks used for Mg (green), Si (red), Ti (blue) and Ca (yellow) lines to be used as sensors in the *Cannon*.

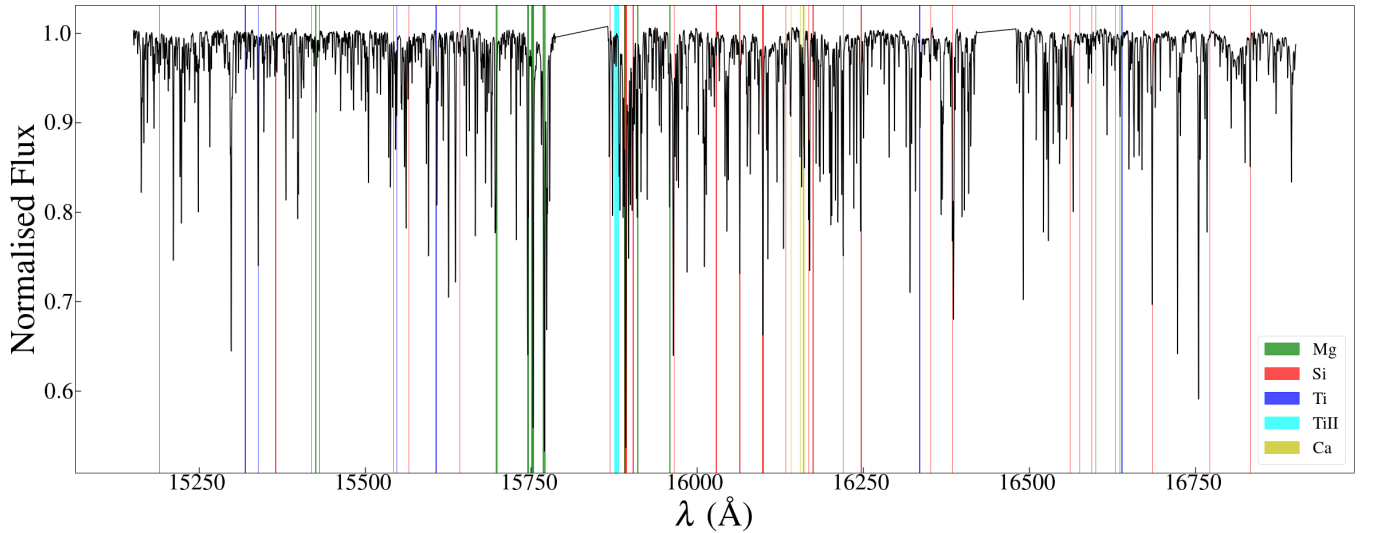


Figure 5. An example of APOGEE spectra (black) covering the wavelength range from ~ 15000 to ~ 17000 Å in 3 chips with gaps in between. We show here the spectra after few Å wavelengths from the edges of each chip have been removed due to issues with normalisation. Different colours indicate the masks used for Mg (green), Si (red), Ti (blue) and Ca (yellow) lines to be used as sensors in the *Cannon*.

3.3 Training and Cross-Validation

Signal-to-noise ratio distribution of the selected training set and that for the whole sample of corresponding survey is shown in the Figure 3. It is clear that GALAH spectra has 4 times lower SNR compared to APOGEE and our chosen training set spectra have SNRs higher than 50th percentile value of the whole distributions.

Once the training set is finalised, we proceed to carry out the training and cross validation for APOGEE-GALAH (training *Cannon* model on APOGEE spectra with GALAH labels) and GALAH-APOGEE (training *Cannon* model on GALAH spectra with APOGEE labels). We get continuum-normalised GALAH spectra sampled onto a common wavelength grid from the spectra fits files. For APOGEE, we have spectra in a common rest frame and identical

wavelength solution, while continuum normalisation is carried out using the normalisation method with the *Cannon* described in Ness et al. (2015). In short, we start with an initial pseudo continuum normalisation using a polynomial fit to the upper 90 percentile of pixels from a running quantile across 50 Å of APOGEE spectra in the training set. We train this set of reference stars with such pseudo continuum normalised spectra using the *Cannon* to generate a *Cannon* model and determine the ‘true’ continuum pixels (flux level ~ 1 and independent of stellar labels) from the model’s baseline spectrum. Finally, we normalise APOGEE spectra by fitting a 2nd order Chebyshev polynomial to these chosen continuum pixels.

While we use the whole spectral wavelength range for training and determining label coefficients for T_{eff} , $\log g$, $[\text{Fe}/\text{H}]$, ν_{micro} .

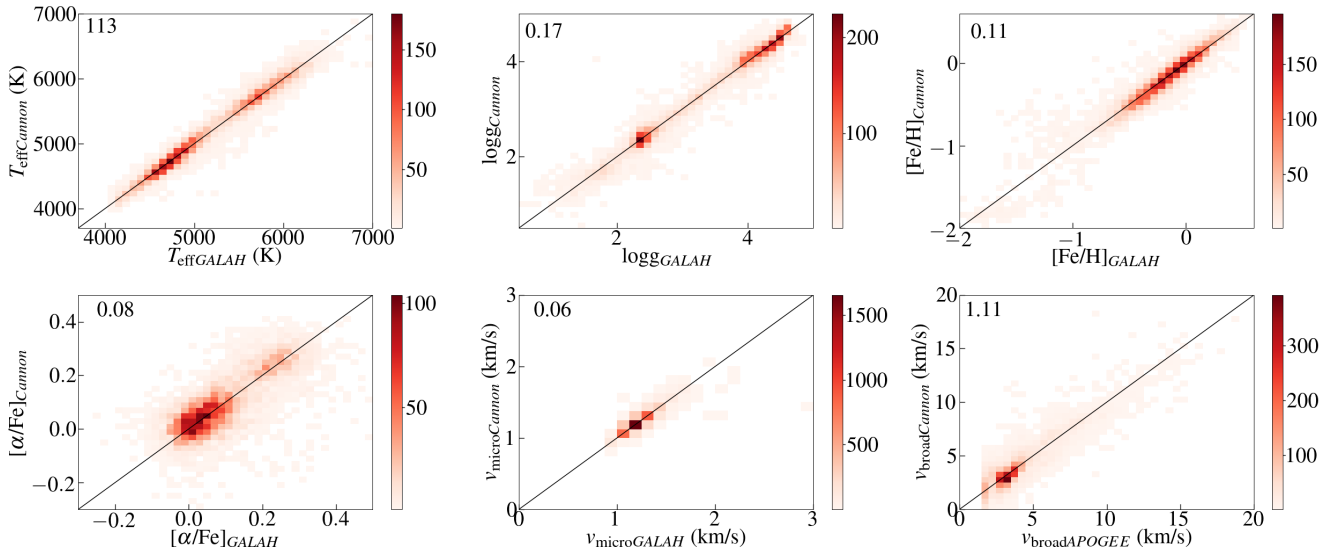


Figure 6. One-to-one relation of GALAH SME stellar labels (x-axis) versus corresponding values derived by the *Cannon* (y-axis) after carrying out a 12-fold cross validation test on the APOGEE-GALAH training set. The dispersion/deviation in each label is indicated on the top left hand side of each plot. The data are binned in the form of 2d histogram colour coded by the number of stars in each bin. Except for the training set boundary limits, the values predicted by the *Cannon* follow a tight one-to-one relation for T_{eff} , $\log g$, $[\text{Fe}/\text{H}]$ and v_{micro} . There is much more scatter in the case of $[\alpha/\text{Fe}]$ and v_{broad} (from APOGEE) values predicted by the *Cannon*, though the majority of them follow the one-to-one relation.

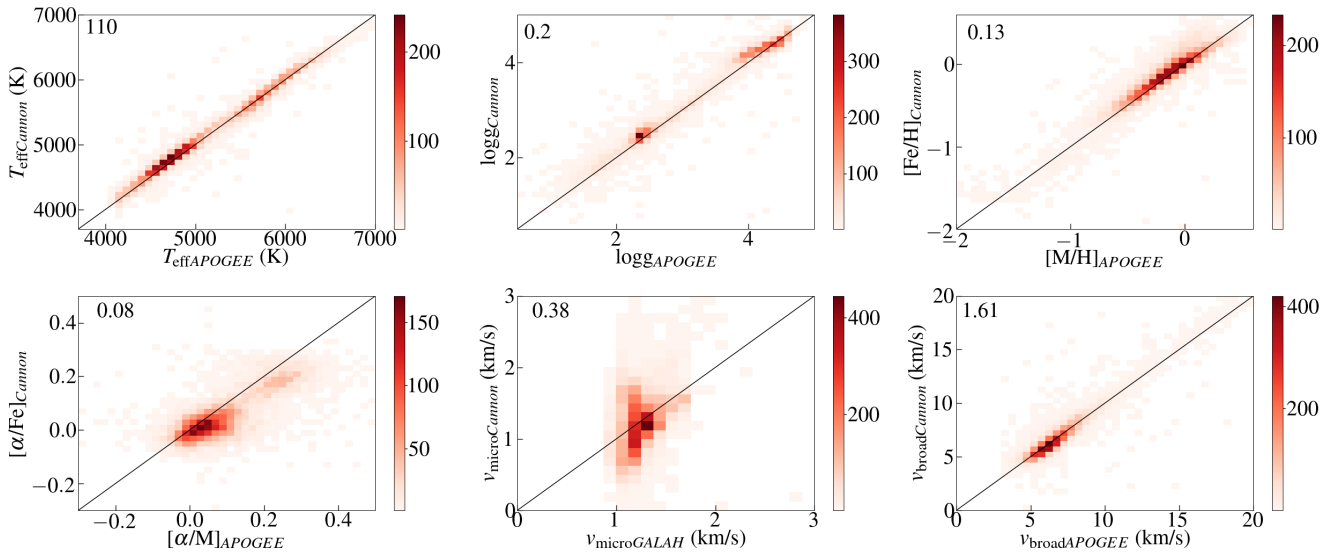


Figure 7. One-to-one relation of APOGEE ASPCAP stellar labels (x-axis) versus corresponding values derived by the *Cannon* (y-axis) after carrying out a 12-fold cross validation test on the GALAH-APOGEE training set. The data are binned in the form of 2d histogram colour coded by the number of stars in each bin. In this case, a tight one-to-one relation is followed by T_{eff} and v_{broad} (from GALAH). The *Cannon* overpredicts $\log g$ for red clumps and dwarfs. Similarly we also find a slight overprediction of $[\text{Fe}/\text{H}]$, while $[\alpha/\text{Fe}]$ is underpredicted for $[\alpha/\text{M}] > \sim 0.05\text{--}0.1$ dex. There is a clear problem in the prediction of v_{micro} by the *Cannon* as indicated by the large dispersion and deviation from the one-to-one relation.

and v_{broad} , we make use of censoring in the case of $[\alpha/\text{Fe}]$. $[\alpha/\text{Fe}]$ for GALAH is determined from an error-weighted combination of selected lines of Si, Mg, Ti and Ca, while APOGEE $[\alpha/\text{M}]$ is determined from a combination of O, Mg, Si, S, Ca, Ti, and Ti II lines. We decided to use line masks for the common elements in both surveys

(Si, Mg, Ti and Ca) to be used as censors in the training step. In the case of GALAH, the line masks for Si, Mg, Ti and Ca are available in the linelist used to determine respective abundances with SME (see Figure 4; Table. A2 in Buder & The GALAH Team 2020). For APOGEE, Jönsson et al. (2020) provides the windows and weights

used in the determination of stellar abundances in their Table 3. We select the wavelength windows for Si, Mg, Ti, Ca lines as shown in the Figure 5.

In the case of APOGEE-GALAH, we use GALAH parameters for all labels except for v_{broad} which characterises the line broadening and hence we use the value provided by APOGEE (v_{sini} for dwarfs, v_{macro} for giants). Similarly we use APOGEE parameters for all labels except for v_{broad} in the case of GALAH-APOGEE.

In order to verify how well the *Cannon* model is able to recover the training set labels, we carry out cross validation by 12-fold cross validation method. For this, we create twelve random subgroups from the training set, then use them individually as test set while the remaining eleven are treated as the training data. We show the resulting one-to-one relation, i.e., predicted label values vs input label values for APOGEE-GALAH and GALAH-APOGEE in Figures 6 and 7 respectively. The dispersion/standard deviation of the difference for each label is indicated in the top left of the respective plots. In the case of APOGEE-GALAH, all labels except $[\alpha/\text{Fe}]$ follow a tight one-to-one relation, though there are deviations in ranges where the number density is low (for example, hottest and coolest values, super giants and $[\text{Fe}/\text{H}] < -1.5$ stars). The relation is not as tight in the case of $[\alpha/\text{Fe}]$ with a low dispersion of 0.08, with deviations becoming prominent at the high and low- α edges. A slightly different relation is seen for $\log g$, $[\alpha/\text{Fe}]$ and v_{micro} in the case of GALAH-APOGEE as can be seen in Figure 7. There is high dispersion ~ 0.38 for v_{micro} that spans the whole APOGEE v_{micro} range. While the one-to-one relation for $\log g$ is tight, *Cannon* predicted values are slightly higher for red clump stars and dwarfs. This could be attributed to the bad v_{micro} estimated for dwarfs by APOGEE and relatively high dispersion in the *Cannon* prediction. The *Cannon* underpredicts $[\alpha/\text{Fe}]$ for $[\alpha/\text{Fe}]_{\text{APOGEE}} > 0.1$. The T_{eff} relation is tighter with the dispersion ~ 110 K, while slight overprediction with higher dispersion is seen for $[\text{Fe}/\text{H}]$. Over all, we see the deviation growing stronger in the low number density borders for each label.

3.4 Testing

We proceed to use the *Cannon* models after training and cross validation for APOGEE-GALAH and GALAH-APOGEE to predict the respective labels for 473,311 APOGEE spectra (in the case of APOGEE-GALAH) and 670,392 GALAH spectra (in the case of GALAH-APOGEE). Since there are limitations in the range covered by the labels in the training set, we remove the predicted labels that lie outside these ranges. In addition, we use the limits in the systematic difference (shown in Figures 1 and 2) as another criterion to choose the stars that pass through to the final catalogue of GALAH scaled APOGEE spectra (APOGEE-GALAH) and APOGEE scaled GALAH spectra (GALAH-APOGEE).

In the case of APOGEE-GALAH, we first remove spectra that had their selected STARFLAG bits set (see Section 3.2.1) to make sure we avoid bad spectra. We then use Figure 1 as a reference from which we use the median value of the systematic difference (APOGEE - GALAH) in bins of 150 K for T_{eff} , 0.15 dex for $\log g$, $[\text{Fe}/\text{H}]$ and $[\alpha/\text{Fe}]$ to define a contour for each case. We then choose the *Cannon* predicted values that lie inside this contour for each of the above mentioned stellar parameters and finally have 222,217 APOGEE spectra with GALAH scaled stellar parameters. We carry out the same exercise for GALAH-APOGEE using Figure 2 as the reference, selecting 527,773 GALAH spectra with APOGEE scaled stellar parameters. The systematic difference plots for the *Cannon* predicted values chosen in this manner are shown in Figures 8 and 9 for APOGEE-GALAH and GALAH-APOGEE respectively.

The trends seen in the case of APOGEE-GALAH training set systematic differences are reproduced by the *Cannon* predictions for rest of the APOGEE spectra except close to the training set border limits, in the case of T_{eff} and $[\alpha/\text{Fe}]$. The $\log g$ values from the *Cannon* are slightly higher for red clump stars compared to that seen in Figure 1(b). $[\text{Fe}/\text{H}]$ difference trend for giants show slight increase in the *Cannon* prediction (though APOGEE values are still higher) compared to APOGEE in the super solar *Cannon* predicted regime, which is opposite to the trend seen for the training set (Figure 1(c)). This is evident in the cross validation plots of APOGEE-GALAH (Figure 6). There are slight differences in the trends seen in the case of GALAH-APOGEE *Cannon* prediction compared to the one seen in Figure 2, especially for $\log g$ and $[\alpha/\text{Fe}]$. This difference is again consistent with that seen in the cross validation. We find the $\log g$ trends for red clump and dwarfs to be shifted a bit towards the right and down in Figure 9b compared to Figure 2(b), which indicates that the *Cannon* over predicts $\log g$ for them. Similarly, we see the *Cannon* predicted $[\alpha/\text{Fe}]$ to be lower (shifted left) for high- α giants in Figure 9(d) compared to Figure 2(d) suggesting under prediction of $[\alpha/\text{Fe}]$ by the *Cannon*. $[\text{Fe}/\text{H}]$ predicted by the *Cannon* seems to exhibit similar trend as seen in the case of the training set.

As mentioned in Section 1, the objective of this work is to combine APOGEE and GALAH, for which we scale APOGEE in terms of GALAH and vice-versa. So it is ideal if we use the *Cannon* to model and predict the same stellar labels for APOGEE spectra using the APOGEE-GALAH training set and GALAH spectra using the GALAH-APOGEE training set. In this case, we use GALAH parameters to train GALAH spectra (APOGEE-GALAH) and APOGEE parameters to train APOGEE spectra (GALAH-APOGEE). Hence we trim down the APOGEE-GALAH training sets by removing GALAH spectra with normalisation issues in chip 4 leading to reducing the training set from 5739 to 5166 stars/spectra. Similarly, we have to add stars to the GALAH-APOGEE training set (since we use APOGEE spectra with APOGEE labels and hence GALAH spectra issues are irrelevant) leading to an increase in the number of stars/spectra from 6817 to 7302. Thus we use these updated training sets to train and generate respective *Cannon* models, which are then used to predict stellar parameters for GALAH spectra (using GALAH SME labels) and APOGEE spectra (using APOGEE ASPCAP labels). From the resulting catalogues, we first remove APOGEE stars with bad spectra based on their selected STARFLAG bits, then proceed to select those *Cannon* values that are within the range covered by the four stellar parameter labels in the respective training set. Finally, we have 301,830 APOGEE spectra with *Cannon* predicted labels by *Cannon* model trained with APOGEE ASPCAP labels and 624,714 GALAH spectra with *Cannon* predicted labels by *Cannon* model trained with GALAH SME labels.

To avoid confusion resulting from the use of two surveys and their spectra in different combinations in this work, hereafter we introduce the following naming convention: *spectra_method_survey*, i.e., *APOGEE Cannon GALAH SME* implies APOGEE spectra trained by the *Cannon* using GALAH SME parameters, and *APOGEE Cannon APOGEE ASPCAP* implies APOGEE spectra trained by the *Cannon* using APOGEE ASPCAP parameters. We show $\log g$ vs T_{eff} (top row) and $[\alpha/\text{Fe}]$ vs $[\text{Fe}/\text{H}]$ (bottom row) plots of training sets (left panel), *Cannon* estimates (middle panel) and corresponding survey estimates (right panel) in Figures 10, 11, 12 and 13 corresponding to *APOGEE Cannon GALAH SME*, *GALAH Cannon GALAH SME*, *GALAH Cannon APOGEE ASPCAP* and *APOGEE Cannon APOGEE ASPCAP* respectively for stars with valid GALAH SME, APOGEE ASPCAP parameters.

As seen in the cross validation and subsequent systematic dif-

APOGEE [DR16] - GALAH Cannon [DR3] (222127)

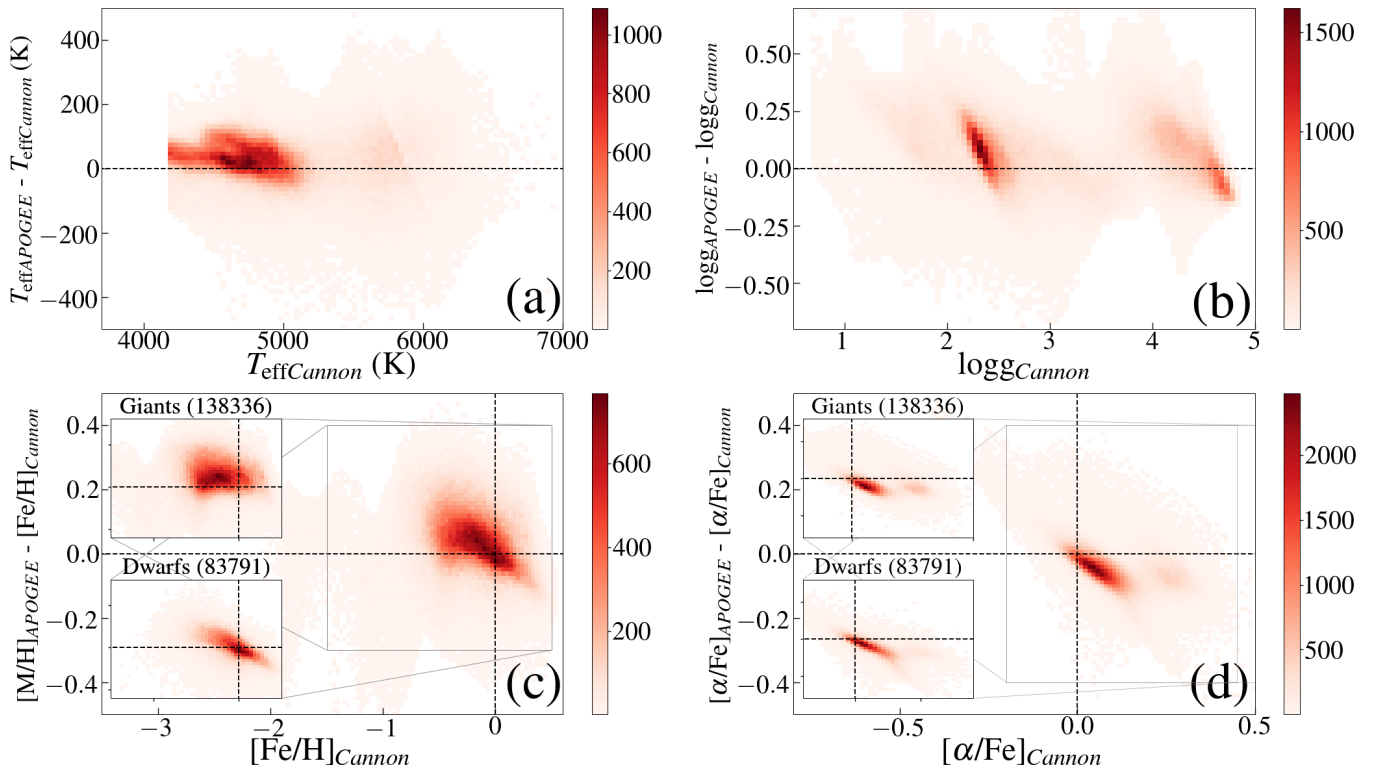


Figure 8. Same as Figure 1 except that we use the stellar parameters derived by the *Cannon* after using the *Cannon* model, trained with the APOGEE-GALAH training set, on APOGEE spectra. The sample shown here is after we have carried out a preliminary selection of the *Cannon* derived stellar parameters that lie within contours defined using the median value of the systematic difference (APOGEE - GALAH) (Figure 1) in bins of 150 K for T_{eff} , 0.15 dex for $\log g$, $[\text{Fe}/\text{H}]$ and $[\alpha/\text{Fe}]$ and after removing bad spectra with selected STARFLAG bits set (see Section 3.2.1). The difference trends are reproduced well by the rest of the APOGEE sample with the *Cannon* model for T_{eff} and $[\alpha/\text{Fe}]$, except at the training set edges, as it is seen in the cross validation step. The $\log g$ values from the *Cannon* are slightly higher for red clump stars compared to that seen in Figure 1(b). The $[\text{Fe}/\text{H}]$ difference trend for giants show slight increase in the *Cannon* prediction (though APOGEE values are still higher) compared to APOGEE which is opposite to the trend seen for the training set (Figure 1(c)).

ference trends, the *Cannon* prediction reproduces the training set features at all regions except at edges in all cases. This is evident in the Kiel diagram as well as $[\alpha/\text{Fe}]$ vs $[\text{Fe}/\text{H}]$ plots. In addition to that, GALAH scaled APOGEE red clump (Figure 10) is puffed up, i.e. higher $\log g$ dispersion, with slight decrease in $\log g$ with increase in T_{eff} compared to almost constant $\log g$ for red clump in APOGEE ASPCAP sample (Figure 10 right panel). This slight slant of red clump is evident in the GALAH training set as well as GALAH SME sample (Figure 11 right panel). As seen in the training set, the high- α and low- α stars are densely populated in comparatively broad ranges of 0.0-0.2 dex and 0.2-0.35 dex respectively in the *Cannon* prediction (Figure 10 bottom middle), while they have much narrower distribution in the APOGEE ASPCAP sample (Figure 10 bottom right). We also find GALAH scaled metal rich ($[\text{Fe}/\text{H}] > 0.0$ dex) stars to have almost constant $[\alpha/\text{Fe}]$ ($\sim 0-0.05$ dex) as seen in the APOGEE ASPCAP sample. There is a sudden number density transition indicating the lower number of hot stars ($T_{\text{eff}} > 5900$ K) for the APOGEE ASPCAP sample, which is a suggested cut by APOGEE to remove poorly determined hot star parameters. There is also a clear difference between the $\log g$ of the cool dwarfs ($T_{\text{eff}} < 4500$ K), with the $\log g$ for GALAH scaled APOGEE increasing slightly with decrease in T_{eff} while in the case of APOGEE ASPCAP, $\log g$ remains constant from

4300-5000 K and increases for cooler stars. This can be attributed to the training set limit effect that we have seen in the cross validation.

When we use GALAH SME parameters to train GALAH spectra, the resulting $\log g$ vs T_{eff} (Figure 11 top middle) and $[\alpha/\text{Fe}]$ vs $[\text{Fe}/\text{H}]$ (Figure 11 bottom middle) is sharper than in the GALAH SME, indicating the *Cannon* predictions to be more precise. The stripes seen at regular T_{eff} intervals, that indicates the piling up of SME predicted T_{eff} s at the model grid edges is absent in the *Cannon* prediction. We also see clear bimodality in $[\alpha/\text{Fe}]$, owing to the higher precision of the *Cannon* prediction. The slight over density of solar $[\alpha/\text{Fe}]$ stars at ~ -0.3 dex $[\text{Fe}/\text{H}]$ in the *Cannon* predicted sample (bottom middle panel in Figure 11) belong to the hot (>6500 K) stars, that have fewer lines/features in their spectra making it hard for the SME to derive accurate abundances and the *Cannon* to predict precise label values. In addition, the cool ($T_{\text{eff}} < 4500$ K) and hot ($T_{\text{eff}} > 6500$ K) dwarf parameters from the *Cannon* show expected training set limitation effects, suggesting that they are not as reliable.

We have seen in the cross validation and subsequent systematic difference trends for GALAH-APOGEE or *GALAH Cannon APOGEE ASPCAP*, how the *Cannon* over predicts and under predicts $\log g$ (for dwarfs) and $[\alpha/\text{Fe}]$ (in $> 0.05-0.1$ dex range) respectively, which we assume is due to the poor estimation of v_{micro} for dwarfs. This is

GALAH [DR3] - APOGEE Cannon [DR16] (527773)

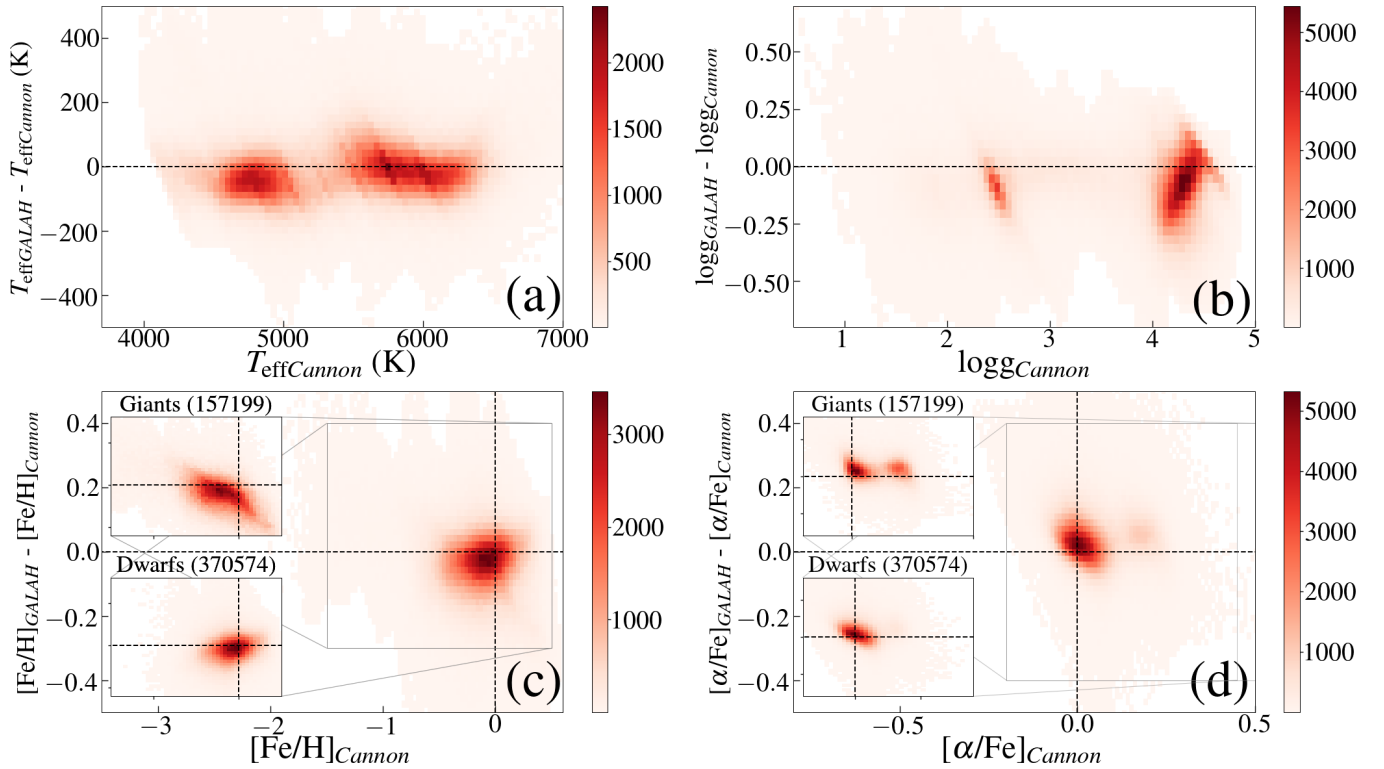


Figure 9. Same as Figure 2 except that we use the stellar parameters derived by the *Cannon* after using the *Cannon* model, trained with the GALAH-APOGEE training set, on GALAH spectra. The sample shown here is after we have carried out a preliminary selection of the *Cannon* derived stellar parameters that lie within contours defined using the median value of the systematic difference (APOGEE - GALAH) (Figure 1) in bins of 150 K for T_{eff} , 0.15 dex for $\log g$, $[\text{Fe}/\text{H}]$ and $[\alpha/\text{Fe}]$. The $\log g$ trends for red clump and dwarfs are shifted a bit towards the right and down (b) compared to that in Figure 2(b), which indicates that the *Cannon* over predicts $\log g$ for them. Similarly, the *Cannon* predicted $[\alpha/\text{Fe}]$ are lower (shifted left) for high- α giants (d) compared to that in Figure 2(d) suggesting under prediction of $[\alpha/\text{Fe}]$ by the *Cannon*. Both the above mentioned effects were seen in the cross validation step.

reflected in the $\log g$ vs T_{eff} (Figure 12 top middle) and $[\alpha/\text{Fe}]$ vs $[\text{Fe}/\text{H}]$ (Figure 12 bottom middle) trends. The $\log g$ upturn for cool dwarfs that we see in the rest of the *Cannon* predictions is not seen here, rather the $\log g$ goes on increasing with decrease in T_{eff} . Similarly $[\alpha/\text{Fe}]$ values for metal rich stars decreases and we do not see a constant $[\alpha/\text{Fe}]$ value as seen in both GALAH SME and APOGEE ASPCAP samples.

The $\log g$ predictions for APOGEE spectra trained with APOGEE labels (Figure 13 top middle panel) results in a puffed up red clump that also seem to be restricted to just below $T_{\text{eff}} < \sim 5200$ K. The $\log g$ predictions for dwarfs are narrow and seems to decrease with decrease in T_{eff} for cool stars and thus turn up in the Kiel diagram. Meanwhile, $[\alpha/\text{Fe}]$ vs $[\text{Fe}/\text{H}]$ (Figure 13 bottom middle panel) trend prediction seems to follow the APOGEE ASPCAP trend, though less precise. This could possibly be attributed to the use of censoring or masking of selected $[\alpha/\text{Fe}]$ lines in the APOGEE spectra which are not the exact same lines used by APOGEE ASPCAP determinations.

The *Cannon* provides covariance errors that are very small, so we follow Buder et al. (2018) where they estimate error from *Cannon* results by comparing the difference of the label input (SME/ASPCAP) and the *Cannon* output as a function of the training set SNR and fit an exponential function to the mean values within the defined SNR bins. For lower SNRs, they do an extrapolation. In our case, we have

four training sets, two each for GALAH and APOGEE. Our training sets have SNR limits of 25 for GALAH and 80 for APOGEE. We bin GALAH SNRs from 25 to 175 with 30 as the bin size, while APOGEE SNRs are binned with bin size of 40 in between 80 and 520.

Overall, the plots discussed above and the similarity of the systematic difference trends to that seen in the training set show how well we have been able to use the *Cannon* in order to derive GALAH scaled stellar parameters from APOGEE spectra and APOGEE scaled parameters from GALAH spectra. We further use a chi square cut (< 8 for APOGEE spectra and < 1 for GALAH spectra), that indicate roughly how closely the *Cannon* model, using the predicted labels for a given star, is able to reproduce that star's spectrum. In addition, we remove cool (< 4500 K) and hot (> 6500 K) dwarfs, stars for which *Cannon* estimates $[\text{Fe}/\text{H}] < -1.5$, APOGEE SNR < 80 and GALAH SNR < 25 . This leads to 482,054 stars/spectra with *Cannon* prediction by using GALAH parameters as the input label, i.e. GALAH scaled, and 503,081 stars/spectra with *Cannon* prediction by using APOGEE parameters as the input label, i.e. APOGEE scaled. The table schema for these two catalogues are described in Table 1. A cross match between the two catalogues by using a unique id (subject_id for GALAH and APOGEE_UniqueID for APOGEE) yields a total of 468,690 stars/spectra that are common to both the

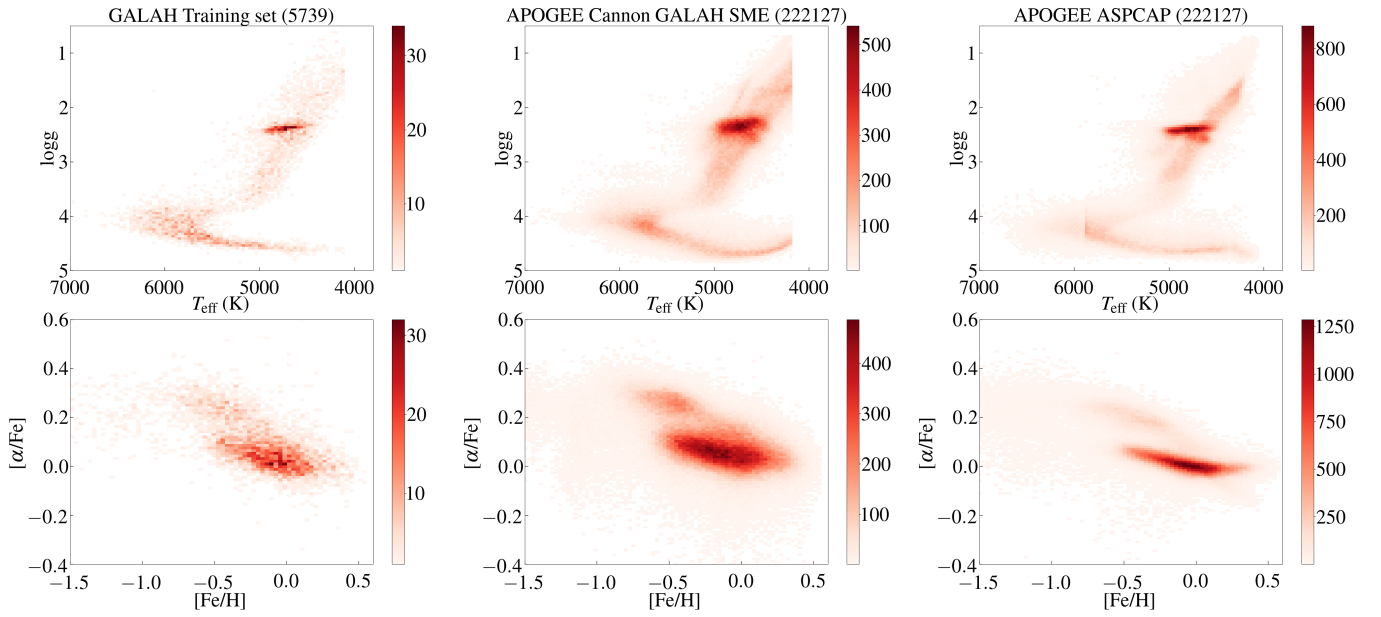


Figure 10. $\log g$ vs T_{eff} (top row) and $[\alpha/\text{Fe}]$ vs $[\text{Fe}/\text{H}]$ (bottom row) plots of GALAH training set (left panel) used to train *Cannon* model on APOGEE spectra with GALAH SME labels, *Cannon* estimates from the test set of APOGEE spectra (middle panel) and APOGEE ASPCAP parameters for the same test set stars (right panel). The data is binned in the form of 2d histogram colour coded by the number of stars in each bin.

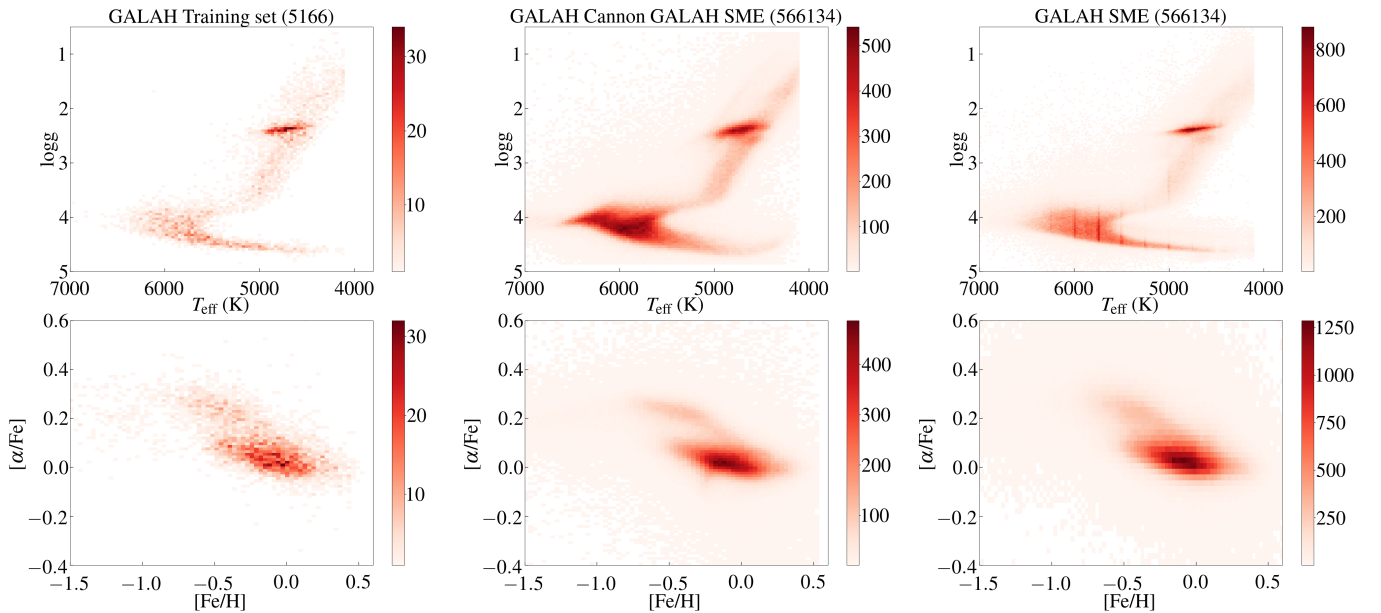


Figure 11. $\log g$ vs T_{eff} (top row) and $[\alpha/\text{Fe}]$ vs $[\text{Fe}/\text{H}]$ (bottom row) plots of GALAH training set (left panel) used to train *Cannon* model on GALAH spectra with GALAH SME labels, *Cannon* estimates from the test set of GALAH spectra (middle panel) and GALAH SME parameters for the same test set stars (right panel). The data is binned in the form of 2d histogram colour coded by the number of stars in each bin.

catalogues. We use this catalogue in order to compare the GALAH scaled and APOGEE scaled metallicity distribution function (MDF), radial metallicity gradient, vertical metallicity gradient and $[\alpha/\text{Fe}]$ vs $[\text{Fe}/\text{H}]$ trends spanning the disc of the Milky Way.

4 RESULTS

4.1 Comparison of Milky Way disc trends

One of the main advantages of combining two complementary surveys like APOGEE and GALAH is the resulting large coverage in Galactocentric distance, R , and average height away from the plane, $|Z|$. We have to make an additional cut on *Gaia* parallaxes for the stars in our catalogue to estimate reliable distances. We make sure to

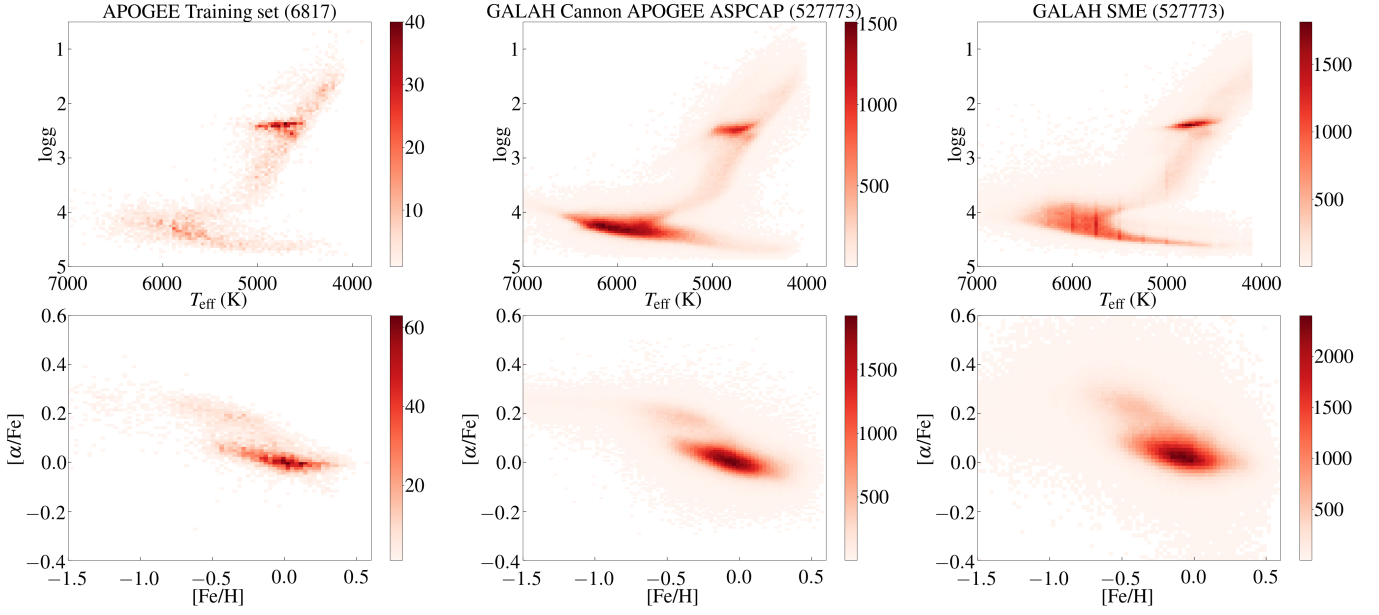


Figure 12. $\log g$ vs T_{eff} (top row) and $[\alpha/\text{Fe}]$ vs $[\text{Fe}/\text{H}]$ (bottom row) plots of APOGEE training set (left panel) used to train *Cannon* model on GALAH spectra with APOGEE ASPCAP labels, *Cannon* estimates from the test set of APOGEE spectra (middle panel) and GALAH SME parameters for the same test set stars (right panel). The data is binned in the form of 2d histogram colour coded by the number of stars in each bin.

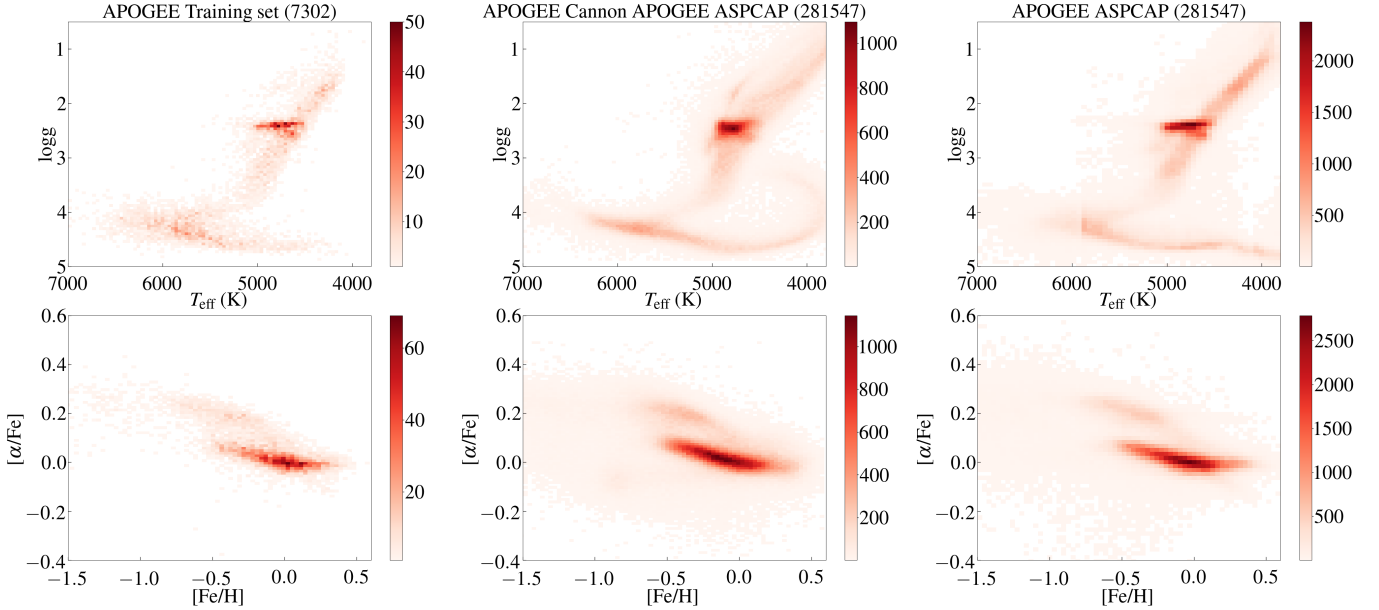


Figure 13. $\log g$ vs T_{eff} (top row) and $[\alpha/\text{Fe}]$ vs $[\text{Fe}/\text{H}]$ (bottom row) plots of APOGEE training set (left panel) used to train *Cannon* model on APOGEE spectra with APOGEE ASPCAP labels, *Cannon* estimates from the test set of APOGEE spectra (middle panel) and APOGEE ASPCAP parameters for the same test set stars (right panel). The data is binned in the form of 2d histogram colour coded by the number of stars in each bin.

select stars with parallax > 0 and fractional parallax error percentage less than 20 per cent resulting in 436,470 stars/spectra. We use the distances estimated by Bailer-Jones et al. (2018) for *Gaia* DR2 stars, that are provided in the GALAH DR3 and APOGEE DR16 catalogues. With this information, we estimated R and Z values for stars in our catalogue and their R-Z distribution is shown in the Figure 14. While there is a good coverage above and below the Galactic mid plane, the inner regions of the Galactic mid plane is lacking the

number statistics. Still, we have sufficient number statistics covering 3 to 13 kpc in R and 0 to 3 kpc in |Z| that can be used to compare the metallicity gradients and alpha abundance trends using GALAH scaled and APOGEE scaled estimates at different R and |z| locations across the Galaxy as discussed below.

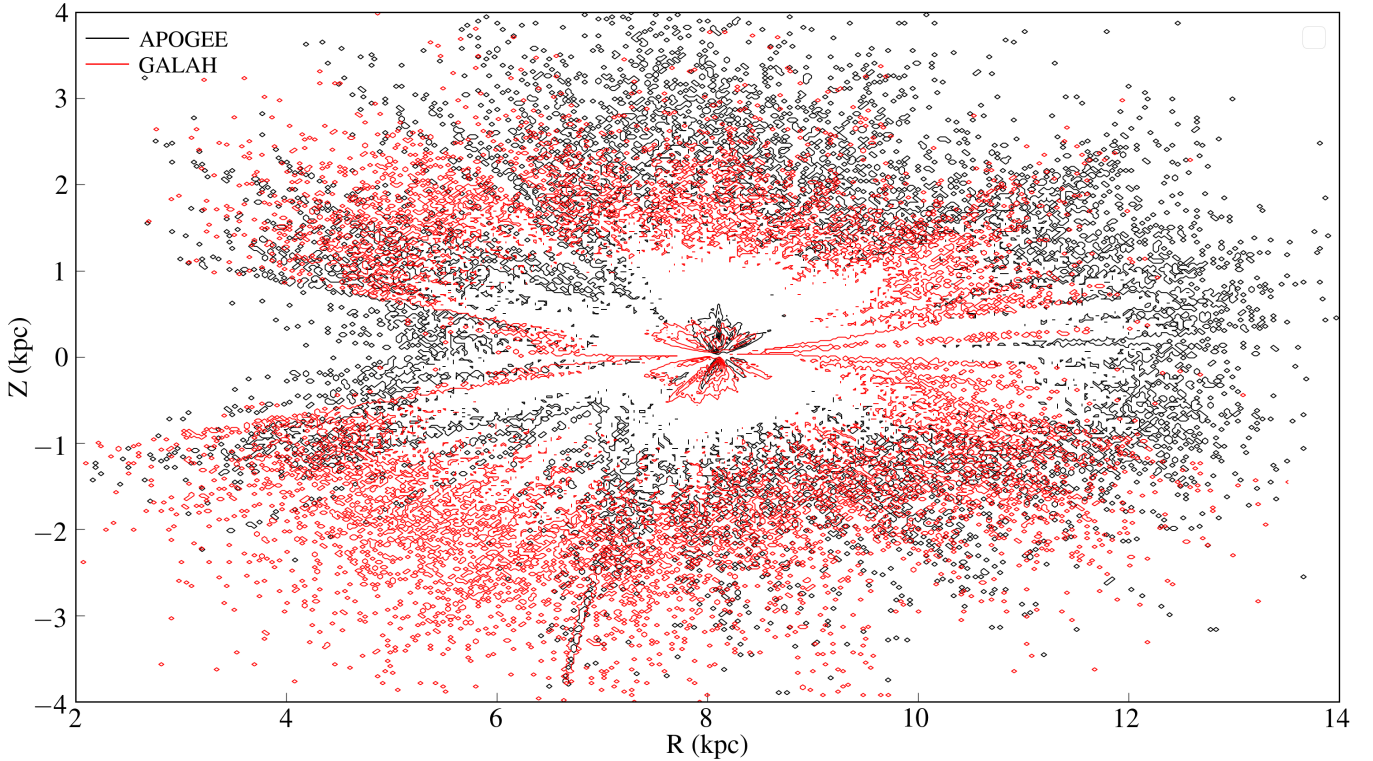


Figure 14. The Z vs R distribution of 444,230 stars with valid *Gaia* DR2 parallaxes and fractional parallax error percentage less than 20 % common to the GALAH scaled (black) and APOGEE scaled (red) stellar parameter catalogues. The parallax cut results in the removal of stars in the inner Milky Way close to the Galactic mid plane, but the whole sample spans a broad R and Z range.

4.1.1 $[Fe/H]$ and $[\alpha/Fe]$ distribution functions

We divide R into bins of 2 kpc from 3 to 13 kpc, and $|Z|$ from 0 to 3 kpc into $[0,0.5],[0.5,1],[1,2]$ and $[2,3]$ kpc bins. We make use of the Gaussian mixture modelling (GMM) with 9 components and the Bayesian Information Criterion (BIC) is used as a cost function to determine the best solution (the one with the lowest BIC value) to the number of Gaussian components that constitutes the distribution to fit. $[Fe/H]$ distributions are binned in 0.1 dex metallicity bins, and $[\alpha/Fe]$ distributions in 0.05 dex $[\alpha/Fe]$ bins in the above mentioned R , $|Z|$ bins as shown in the Figures 15 and 16 respectively. The R increases from left to right and height from the mid plane increases from bottom to top.

The number of stars in each of these R , $|Z|$ bins are indicated in the plots, which show that the inner mid plane ($3 \leq R \leq 5$ kpc) and highest $|Z|$ bin ($2 \leq |Z| \leq 3$ kpc) of inner and outer radial ($11 \leq R \leq 13$ kpc) bins have the lowest number statistics (< 400) mainly attributed to the parallax cut made to the sample. The remaining bins have sufficient statistics that makes the trends and distributions seen in them more trustworthy. We also indicate the mean metallicity that we estimate for APOGEE scaled and GALAH scaled samples in each of the $R, |Z|$ bin plots. In terms of the comparison between the two surveys, mean metallicity of the APOGEE scaled sample in each $R, |Z|$ bin is higher than for GALAH scaled sample, though the magnitude of this difference varies depending on the R and $|Z|$ bins. For example, the difference is consistently lower (< 0.02) for all radial bin samples in the highest $|Z|$ (2 to 3 kpc) bin, while the largest difference (0.08–0.09) is seen for the samples in $R-[3,5]$ $|Z|-[0.5,1]$, $R-[5,7]$ $|Z|-[0.5,1]$ and $R-[5,7]$ $|Z|-[0,0.5]$ samples. In the solar neighborhood ($R-[7,9]$ $|Z|-[0,0.5]$), the GMM fit to both distributions are similar with 0.03

dex difference between the mean values. If we look at the variation of the distribution and the mean values along R and $|Z|$, we find the distribution to shift toward metal poor values as we move away from the Galactic mid plane, while the mean metallicities/peaks of distributions at all heights (except $1 \leq |Z| \leq 2$) tend to increase from the inner regions into the solar neighborhood and starts decreasing from there on to the outer regions. There is also a consistent increase in the narrowness of the distributions from inner to outer regions, which could indicate the lack of mixing happening in the regions outside the solar neighborhood. There are evidences of mixing via radial migration of stars in the negative to positive skewness variation of distributions from inner to outer regions, indicating the excess of metal poor stars in the inner Galaxy and metal rich stars in the outer Galactic mid plane regions. This particular trend was observed and discussed in Hayden et al. (2015), where they used $\sim 70,000$ RGB stars from APOGEE DR12. Using a high resolution N-body + SPH simulation, Loebman et al. (2016) showed that such change in skewness can arise from radial migration. At the same time, in the highest $|Z|$ bin, all distributions are found to be negatively skewed, indicating the presence of metal poor halo stars.

When it comes to the $[\alpha/Fe]$ distributions, the distributions are bimodal in $5 \leq R \leq 11$, $|Z| \leq 2$ kpc regions. Both GALAH scaled and APOGEE scaled distributions seem to be slightly consistent only in the solar neighborhood, while APOGEE scaled distributions are narrower than the GALAH scaled sample distribution and consistently having one of its peak value close to the solar $[\alpha/Fe]$ in the aforementioned region. This offset in the peak value between the two survey scaled samples is seen in all $R, |Z|$ bins. The high α sample is dominant in the inner region and away from the Galactic mid plane,

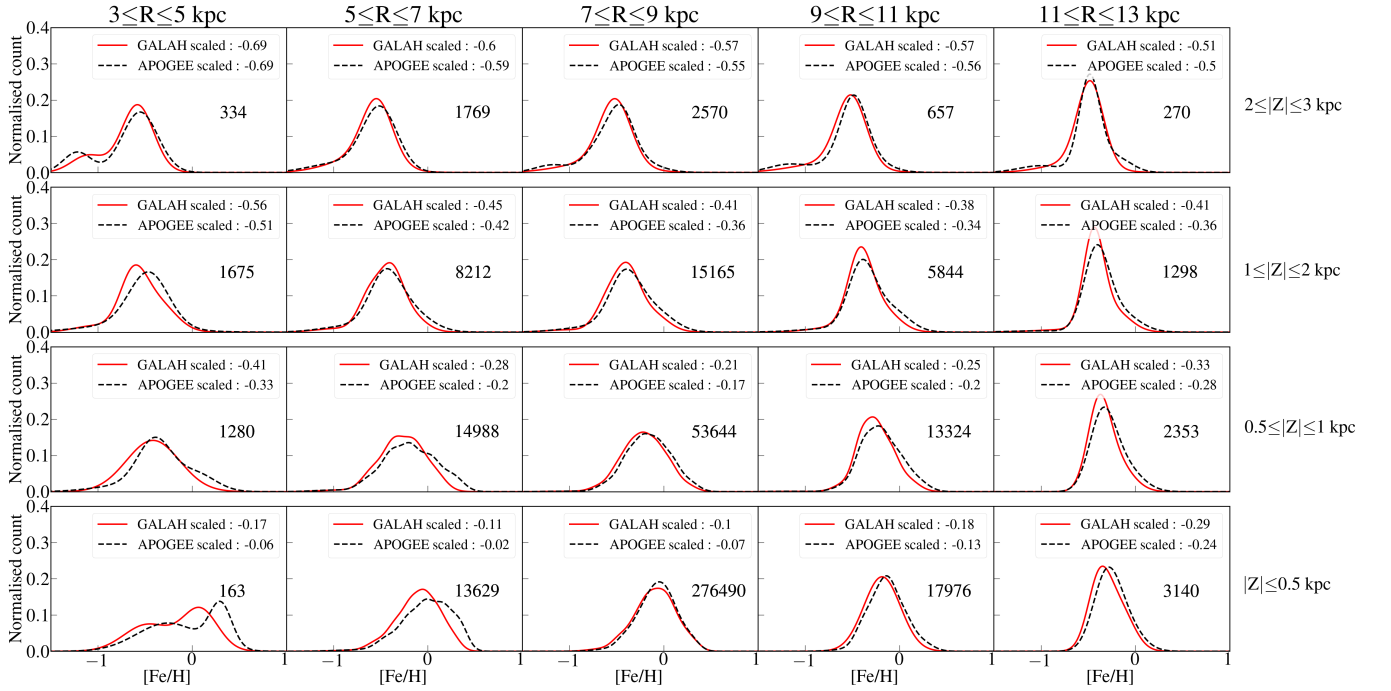


Figure 15. Metallicity distribution function of stars in the GALAH scaled (black line) and APOGEE scaled (black dashed line) sample variation in different Galactic zones, defined by the R and $|Z|$ bins. We divide R into bins of 2 kpc from 3 to 13 kpc (left to right), and $|Z|$ from 0 to 3 kpc into $[0,0.5]$, $[0.5,1]$, $[1,2]$ and $[2,3]$ kpc bins (bottom to top). The distributions in each R , $|Z|$ bin for each sample are fitted using Gaussian mixture modelling (GMM; e.g. [Rojas-Arriagada et al. 2017](#)) in 0.1 dex metallicity bins. The mean value of the distributions are indicated on top right for each survey sample along with the number of stars in each R , $|Z|$ bin. The number statistics is low in inner mid plane ($3 \leq R \leq 5$ kpc) and highest $|Z|$ bin ($2 \leq |Z| \leq 3$ kpc) of inner and outer radial ($11 \leq R \leq 13$ kpc) bins. There is a clear offset between the mean of APOGEE scaled and GALAH scaled samples in most R , $|Z|$ bins with metallicity higher for APOGEE scaled sample.

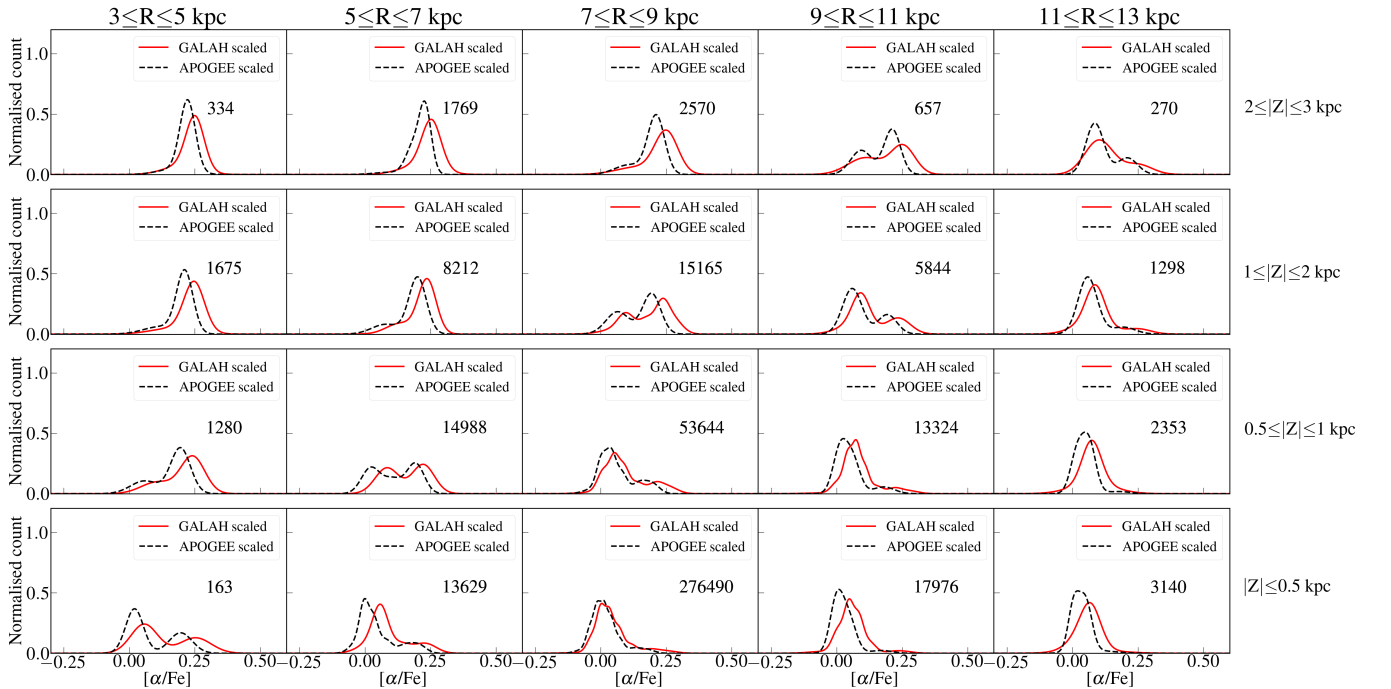


Figure 16. Similar to Figure 15, except for $[\alpha/\text{Fe}]$ with the GMM fit to the sample distribution binned in 0.05 dex $[\alpha/\text{Fe}]$ bins. Clear bi modality in $[\alpha/\text{Fe}]$ distribution is seen in $5 \leq R \leq 11$, $|Z| \leq 2$ kpc regions, with APOGEE scaled sample (black dashed line) exhibiting narrower distribution compared to GALAH scaled sample (black continuous line).

Table 1. Table schema of APOGEE scaled and GALAH scaled stellar parameter catalogues

Column Name	Units	Description
Unique ID		Unique survey star id
ra	deg	Right ascension
dec	deg	Declination
teffCann	K	<i>Cannon</i> estimate of effective temperature
e_teffCann	K	SNR based error of teffCann
loggCann	log(cm/s ²)	<i>Cannon</i> estimate of surface gravity
e_loggCann	log(cm/s ²)	SNR based error of loggCann
fehCann	dex	<i>Cannon</i> estimate of metallicity
e_fehCann	dex	SNR based error of fehCann
alphafeCann	dex	<i>Cannon</i> estimate of $[\alpha/\text{Fe}]$
e_alphafeCann	dex	SNR based error of alphafeCann
vmicroCann	km/s	<i>Cannon</i> estimate of microturbulence
e_vmicroCann	km/s	SNR based error of vmicroCann
vbroadCann	km/s	<i>Cannon</i> estimate of broadening velocity
e_vbroadCann	km/s	SNR based error of vbroadCann
r_chi_sq		reduced chi-square from <i>Cannon</i>
snrCann		Signal-to-noise ratio from <i>Cannon</i>
teff	K	Survey effective temperature
e_teff	K	Survey effective temperature error
logg	log(cm/s ²)	Survey surface gravity
e_logg	log(cm/s ²)	Survey surface gravity error
feh	dex	Survey metallicity
e_feh	dex	Survey metallicity error
alphafe	dex	Survey $[\alpha/\text{Fe}]$
e_alphafe	dex	Survey $[\alpha/\text{Fe}]$ error
vmicro	km/s	Survey microturbulence
e_vmicro	km/s	Survey microturbulence error
vbroad	km/s	Survey broadening velocity
e_vbroad	km/s	Survey broadening velocity error
snr		Survey signal-to-noise ratio
r_est	pc	Estimated distance from Bailer-Jones+18
r_lo	pc	Lower bound from Bailer-Jones+18
r_hi	pc	Higher bound from Bailer-Jones+18
parallax	mas	Gaia DR2 parallax
e_parallax	mas	Gaia DR2 parallax error

while low α sample becomes dominant in the outer regions. This is reflective of the high α thick disc being dominant in the inner Milky Way regions with small scale length and low α thin disc being dominant in the outer Milky Way regions with large scale lengths.

4.1.2 $[\alpha/\text{Fe}]$ vs $[\text{Fe}/\text{H}]$ trends

With the $[\alpha/\text{Fe}]$ vs $[\text{Fe}/\text{H}]$ plots shown in Figure 17, we see the features that we described in Section 4.1.1 in combination, i.e., metal poor high α population is dominant in the inner Milky Way regions and metal rich low α population becomes dominant as we move to the outer regions. The narrowness in the APOGEE scaled $[\alpha/\text{Fe}]$ values, slightly higher $[\alpha/\text{Fe}]$ values for GALAH scaled sample as well as the lower metallicity for GALAH scaled sample is also very evident. We also note the constancy in the high $[\alpha/\text{Fe}]$ trend/ locus in the inner Milky Way regions where they are dominant in both APOGEE scaled (black contours in Figure 17) and GALAH scaled samples (red contours in Figure 17). These trends have been discussed in Hayden et al. (2015); Anders et al. (2014) using APOGEE DR12 and more recently in Weinberg et al. (2019) using APOGEE DR14, and have been attributed to the radial migration mixing stellar populations across the disc. Buck (2020), using cosmological hydrodynamical simulations of Milky Way like galaxies showed that the double se-

Table 2. Radial metallicity gradients at different R, $|Z|$ bins for GALAH scaled and APOGEE scaled samples.

R (kpc)	$ Z $ (kpc)	$\frac{d[\text{Fe}/\text{H}]}{dR}_{\text{GALAH}}$ (dex kpc ⁻¹)	$\frac{d[\text{Fe}/\text{H}]}{dR}_{\text{APOGEE}}$ (dex kpc ⁻¹)
3 - 5	0 - 0.5	0.31 ± 0.08	0.39 ± 0.14
	0.5 - 1	0.18 ± 0.04	0.19 ± 0.04
	1 - 2	0.10 ± 0.02	0.07 ± 0.02
	2 - 3	0.09 ± 0.03	0.13 ± 0.07
5 - 7	0 - 0.5	-0.05 ± 0.01	-0.08 ± 0.01
	0.5 - 1	0.07 ± 0.01	0.05 ± 0.01
	1 - 2	0.02 ± 0.00	0.03 ± 0.01
	2 - 3	0.00 ± 0.01	0.01 ± 0.01
7 - 9	0 - 0.5	-0.03 ± 0.01	-0.04 ± 0.01
	0.5 - 1	-0.01 ± 0.01	0.01 ± 0.01
	1 - 2	0.01 ± 0.01	0.01 ± 0.01
	2 - 3	0.02 ± 0.01	0.01 ± 0.01
9 - 11	0 - 0.5	-0.07 ± 0.01	-0.06 ± 0.01
	0.5 - 1	-0.06 ± 0.01	-0.06 ± 0.01
	1 - 2	-0.01 ± 0.01	-0.02 ± 0.01
	2 - 3	0.02 ± 0.02	0.02 ± 0.02
11 - 13	0 - 0.5	-0.07 ± 0.01	-0.05 ± 0.01
	0.5 - 1	-0.05 ± 0.01	-0.04 ± 0.01
	1 - 2	-0.04 ± 0.01	-0.01 ± 0.01
	2 - 3	-0.06 ± 0.02	-0.02 ± 0.02

quence is the consequence of a gas-rich merger that results in the formation of low- α sequence after a time when the high α sequence have already evolved to high metallicities, followed by migration that has distributed stars radially across the disc. This trend is also consistent with classical Galactic chemical evolution models (e.g. Very recently, Sharma et al. (2020) have been able to reproduce the observed variation of the MDF, their skewness variation and $[\alpha/\text{Fe}]$ vs $[\text{Fe}/\text{H}]$ trends in different Galactic zones with the help of an analytical chemodynamical model with a smooth and continuous star formation history and velocity dispersion relations that includes the effects of radial migration and kinematic heating. They find the constancy of the high $[\alpha/\text{Fe}]$ to be the result of churning wherein stars move outward from the inner Galaxy and the double sequence is attributed to the delay between the onset of star formation and the occurrence of SNIa and the radial migration of stars. Vincenzo & Kobayashi (2020), using their self-consistent cosmological chemodynamical simulation of a MW-type galaxy, have reproduced the observed radial variations of the bi modal distribution in $[\alpha/\text{Fe}]$ vs $[\text{Fe}/\text{H}]$ from APOGEE DR16.

While there have been previous studies that have explored the R, $|Z|$ variation of $[\alpha/\text{Fe}]$ vs $[\text{Fe}/\text{H}]$ trend using APOGEE data (DR12: Hayden et al. 2015, DR14: Weinberg et al. 2019), there have been limitations in the number statistics when we use APOGEE alone. With our work, there are better number statistics at different R, $|Z|$ locations across the Galaxy which will help in further studies involving the modelling of such trends. In addition, our respective survey scaled metallicities and $[\alpha/\text{Fe}]$ values can be used to compare model realisations with observed trends which in themselves are different.

4.1.3 Radial metallicity gradient

Here we estimate and quantify the variation of metallicity as a function of present day Galactocentric radius in the same R, $|Z|$ bins as

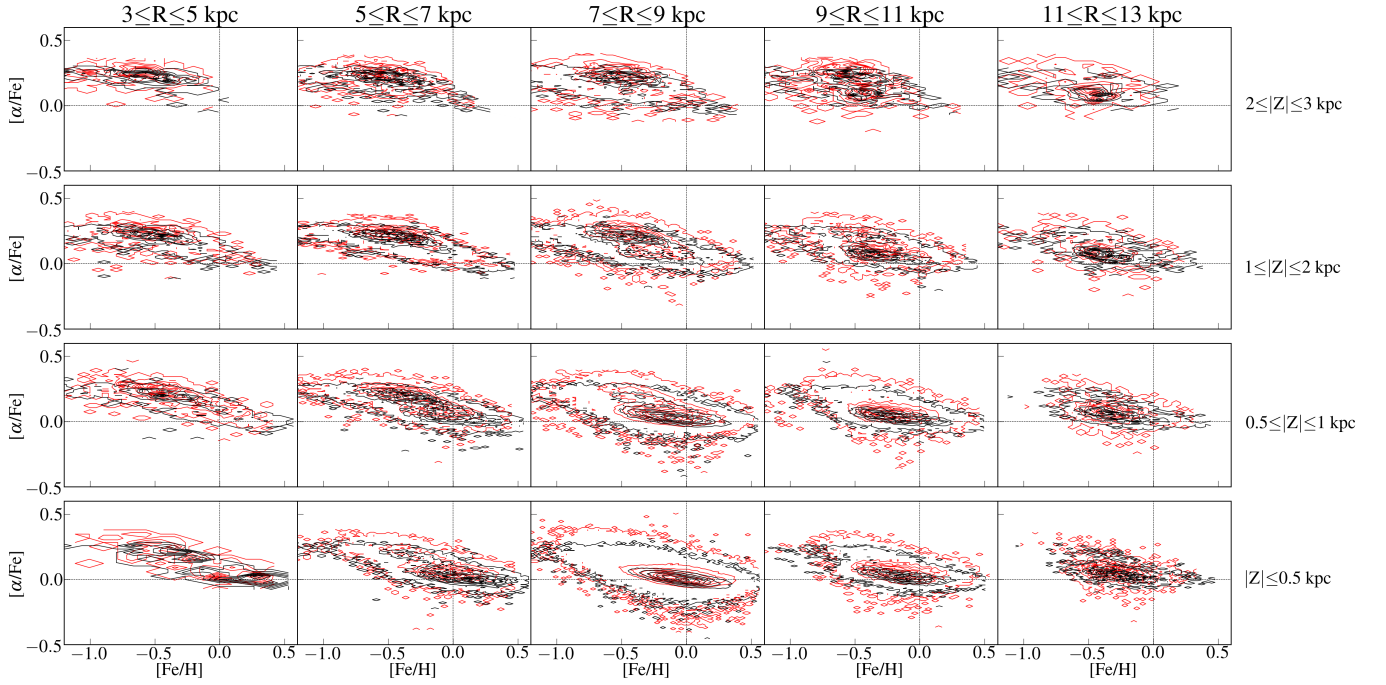


Figure 17. Contour plot showing $[\alpha/\text{Fe}]$ vs $[\text{Fe}/\text{H}]$ trends in the R , $|Z|$ bins as in Figure 15 for GALAH scaled sample (red) and APOGEE scaled sample (black). The horizontal and vertical dashed lines indicate the solar $[\alpha/\text{Fe}]$ and $[\text{Fe}/\text{H}]$ respectively. For both samples, double $[\alpha/\text{Fe}]$ sequence is evident in $5 \leq R \leq 11$, $|Z| \leq 2$ kpc regions though there is a broad dispersion with $[\alpha/\text{Fe}]$ varying from -0.5 to $+0.5$ dex in the case of GALAH scaled sample, while APOGEE scaled sample exhibit much lower dispersion in $[\alpha/\text{Fe}]$ values as seen in Figure 16. In both cases, metal poor high α population is dominant in the inner Milky Way regions and metal rich low α population becomes dominant in the outer regions.

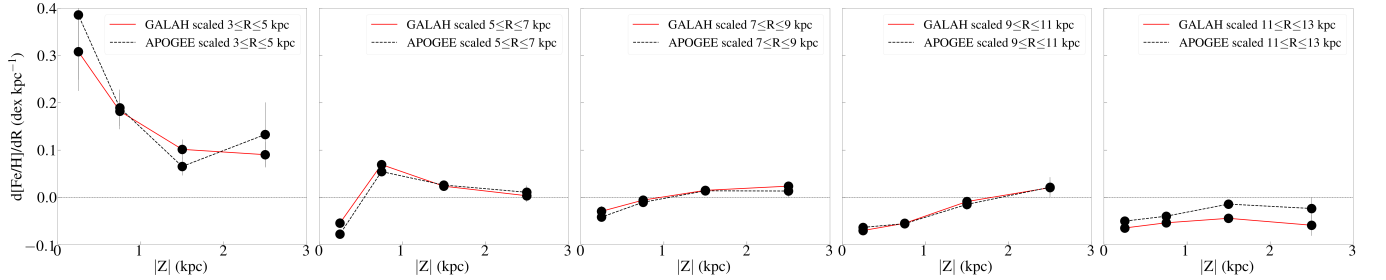


Figure 18. Radial metallicity gradient, $d[\text{Fe}/\text{H}]/dR$, vs height away from the plane, $|Z|$, for APOGEE scaled (black dashed line) and GALAH scaled (black solid line) samples showing the variation of radial metallicity gradient away from the plane. The black dots with the error bars represent the slopes of the gradients measured for stars binned in $|Z|$ in $[0.0.5, 1, 2, 3]$, while each panel from left to right are 2 kpc bins in R from 3 to 13 kpc. The slopes of the gradients within each $|Z|$ bin are measured by finding the median metallicity (black dots) in 0.2 kpc bins in R and then using a linear least-squares regression fit to the median metallicity at each R bins and the error bar is from the line fit to the median values. The black dashed line in each plot represent the flat metallicity gradient value ($d[\text{Fe}/\text{H}]/dR = 0$). There is a consistent transition of radial gradient from negative to flat/positive as we move away from the Galactic mid plane and the gradients are found to change from positive in inner regions to negative in outer regions except close to the mid plane.

used in the MDF, ADF and $[\alpha/\text{Fe}]$ vs $[\text{Fe}/\text{H}]$ trends for APOGEE scaled and GALAH scaled samples in the Figure 18. The black dots with the error bars represent the slopes of the gradients measured for stars binned in $|Z|$ in $[0.0.5, 1, 2, 3]$, while each panel from left to right are 2 kpc bins in R from 3 to 13 kpc. The slopes of the gradients within each $|Z|$ bin are measured by finding the median metallicity (black dots) in 0.2 kpc bins in R and then using a linear least-squares regression fit to the median metallicity at each R bins and the error bar is from the line fit to the median values. Black line and black dashed line represent the variation of the radial metallicity gradient with height away from the plane in each 2 kpc R bin for GALAH

scaled and APOGEE scaled samples respectively. Table 2 lists the radial metallicity gradient estimates in different R , $|Z|$ bins.

As mentioned earlier, the low number statistics in the inner mid plane ($3 \leq R \leq 5$ kpc; First panel of Figure 18) and highest $|Z|$ bin ($2 \leq |Z| \leq 3$ kpc) of inner and outer radial ($11 \leq R \leq 13$ kpc; Last panel of Figure 18) bins makes the gradients estimated in these regions less reliable. This pertains to the slopes estimated for the first and last $|Z|$ bins in the left most plot ($3 \leq R \leq 5$ kpc). In the 5 to 11 kpc radial range, radial metallicity gradients measured using GALAH scaled sample are slightly positive/equal to that measured using APOGEE scaled sample. There is a transition of the gradient from negative values near the mid plane to positive values or becoming flat at heights

away from the plane in these radial ranges, while the gradients are found to change from positive/flat to negative from inner radial bins to outer radial bins except close to the mid plane. The flattening of gradient with height can be attributed to the age dependence of the radial metallicity gradient. [Casagrande et al. \(2011\)](#) and [Anders et al. \(2017\)](#) have shown using solar neighborhood stars and open clusters respectively, that the gradient is negative at young ages turning positive at older ages. Hence comparatively higher number of older stars at higher $|Z|$ results in positive/flatter radial gradient at higher $|Z|$. In the outer radial bin ($11 \leq R \leq 13$ kpc), GALAH scaled sample has slightly steeper negative gradient compared to APOGEE scaled sample and there is no transition from negative to positive as we move away from the plane, though the number statistics in the highest $|Z|$ bin makes the gradient estimate less reliable in this radial bin.

[Hayden et al. \(2014\)](#) have carried out a similar study using APOGEE DR10 sample, finding a similar trend of radial gradient flattening with height. Since they use the previous data release of APOGEE, it is not ideal to compare our estimated gradients with them. After taking into account selection function effects, [Bergemann et al. \(2014\)](#) estimated radial metallicity gradients of -0.068 ± 0.014 dex kpc^{-1} within $|Z|$ of 300 pc and a steeper value of -0.114 ± 0.009 dex kpc^{-1} within $300 < |Z| < 800$ pc using 144 stars in the Gaia-ESO (GES) survey in $6 < R < 9.5$ kpc range. When we make a similar cut in R and $|Z|$ with our samples, we find consistent gradient within $|Z| < 300$ pc (-0.07 ± 0.01 dex kpc^{-1}) with APOGEE scaled sample and slightly shallower slope (-0.03 ± 0.01 dex kpc^{-1}) with our GALAH scaled sample. At higher $|Z|$ bin, our estimates are flatter and close to 0.0 dex kpc^{-1} compared to the GES sample. This can be attributed to the small GES dataset in this bin as mentioned in [Bergemann et al. \(2014\)](#). [Xiang et al. \(2015\)](#), using the main sequence turn off (MSTO) stars from the LAMOST Spectroscopic Survey of the Galactic Anti-center (LSS-GAC), have determined radial gradient that varies from from -0.1 dex kpc^{-1} at $|Z| = 0$ kpc to 0.02 dex kpc^{-1} at $|Z| = 2$ kpc in the radial range of $6 \leq R \leq 13$ kpc. This is consistent with the trend that we see from both samples in our study. Using red clump stars in the LSS-GAC, [Huang et al. \(2015\)](#) estimated a radial metallicity gradient of -0.08 dex kpc^{-1} near the mid plane in the $7 \leq R \leq 11.5$ kpc, that flattens with increasing height as seen in our samples. The above mentioned studies also split their sample based on age proxies (high α , low α in [Hayden et al. 2014](#)) or direct age estimates (in [Xiang et al. 2015](#)) to understand the age based gradient variation. This is currently out of the scope of this paper, where we intend to provide the catalogue and do a comparison study of the Milky Way disc trends between APOGEE scaled and GALAH scaled sample. Many other surveys like RAVE have also been used to explore the radial metallicity gradient with giants ([Boeche et al. 2014](#)) and dwarfs ([Boeche et al. 2013](#)) from RAVE DR4 catalogue. They find the radial metallicity gradient to vary from -0.05 to $+0.05$ dex kpc^{-1} with height using giants in the $4.5 \leq R \leq 9.5$ kpc radial range and ~ -0.029 dex kpc^{-1} using dwarfs within $|Z| \leq 0.4$ kpc in the same radial range. Close to the Galactic mid plane, our estimates from both the sample are consistent with the RAVE estimates, but slightly less positive at larger heights. Meanwhile, we note that the RAVE spectral resolution is comparatively lower than that of GALAH and APOGEE, that can affect their metallicity estimates. Using open clusters in APOGEE DR14 and GALAH DR2, [Carrera et al. \(2019\)](#) estimated a radial metallicity gradient of -0.052 ± 0.003 dex kpc^{-1} in the $6.5 \leq R \leq 13$ kpc radial range, while there is a significant variation in this value for open clusters (between -0.035 dex kpc^{-1} using APOGEE in [Cunha et al. 2016](#) and -0.1 dex kpc^{-1} using GES in [Jacobson et al. 2016](#)). Using homogenised set of stellar parameters and elemental abundances of 134 open clusters in APOGEE

Table 3. Vertical metallicity gradients at different R , $|Z|$ bins for GALAH scaled and APOGEE scaled samples.

R (kpc)	$ Z $ (kpc)	$\frac{d[Fe/H]}{d Z }_{GALAH}$ (dex kpc^{-1})	$\frac{d[Fe/H]}{d Z }_{APOGEE}$ (dex kpc^{-1})
3 - 5	0 - 3	-0.20 ± 0.04	-0.26 ± 0.05
5 - 7	0 - 3	-0.21 ± 0.03	-0.25 ± 0.03
7 - 9	0 - 3	-0.19 ± 0.02	0.20 ± 0.01
9 - 11	0 - 3	-0.16 ± 0.01	-0.16 ± 0.01
11 - 13	0 - 3	-0.09 ± 0.01	-0.11 ± 0.01

DR16 and GALAH DR3, [Spina et al. 2020](#) (submitted) estimated a radial metallicity gradient of -0.076 ± 0.009 dex kpc^{-1} within $6 < R < 18$ kpc. They also find a flatter gradient for younger clusters and steeper for older ones, while the field stars gradient is found to go in the opposite direction ([Anders et al. 2017](#)). They attribute this open cluster trend to the Galactic selection effect by which clusters living near gravitational potentials are disrupted quickly. There are various other metallicity gradient studies using classical cepheids, that are young, ([Minniti et al. 2020](#), [Genovali et al. 2014](#) etc.) that can be compared with our sample once we estimate reliable ages for them. [Vincenzo & Kobayashi \(2020\)](#) have measured radial metallicity gradient between -0.046 and -0.055 dex kpc^{-1} using APOGEE DR16 in the $5 \leq R \leq 10$ kpc, $|Z| \leq 0.5$ kpc range, which they found to be consistent with their model predictions. We estimate values of -0.05 dex kpc^{-1} using APOGEE scaled sample and -0.03 dex kpc^{-1} using the GALAH scaled sample in the same region. This again indicates that there is still room for constraining such models using estimates from multiple surveys.

4.1.4 Vertical metallicity gradient

We estimate the vertical metallicity gradient by employing the same method as in the Section 4.1.3. We find the median metallicity in 0.3 kpc bins in $|Z|$ for $|Z| \leq 3$ kpc within 2 kpc radial bins from 3 to 13 kpc and then use a linear least-squares regression fit to the median metallicity at each $|Z|$ bins, shown in the Figure 19. Table 3 lists the vertical metallicity gradient estimates in different R bins. Both the survey scaled samples exhibit negative vertical metallicity gradients as expected from the mean values and distributions seen in the MDF plots (Section 4.1.1). This negative gradient gradually becomes flatter as we move outwards from the inner regions. The difference in the estimated gradient between APOGEE scaled (dashed line) and GALAH scaled samples are prominently evident in the first two radial bins, where there is also lesser number statistics compared to other radial bins. In the solar neighborhood ($7 \leq R \leq 9$ kpc), both the samples have consistent gradient estimate of ~ -0.20 dex kpc^{-1} , though the median metallicities in the APOGEE scaled sample are higher than in the GALAH scaled sample. There is consistency in the gradient estimate for the two outer most radial bins as well.

A similar study carried out by [Hayden et al. \(2014\)](#) estimated much steeper vertical metallicity gradients using APOGEE DR10 sample for similar radial bins but limited to $|Z| \leq 2$ kpc. The 2 to 3 kpc $|Z|$ bin in our sample is dominated by metal poor stars, that will flatten the slopes compared to the case when we use $|Z| \leq 2$ kpc. The trend of flattening gradient with R is seen in their work as well. Using $\sim 10,511$ red clump stars in the RAVE DR4 catalogue, [Boeche et al. \(2014\)](#) measured a shallower slope of -0.112 ± 0.007 dex kpc^{-1} in the region extending from 7.5 to 8.5 kpc in R and $|Z| \leq 2$ kpc, which is ~ 0.1 dex shallower than our estimates.

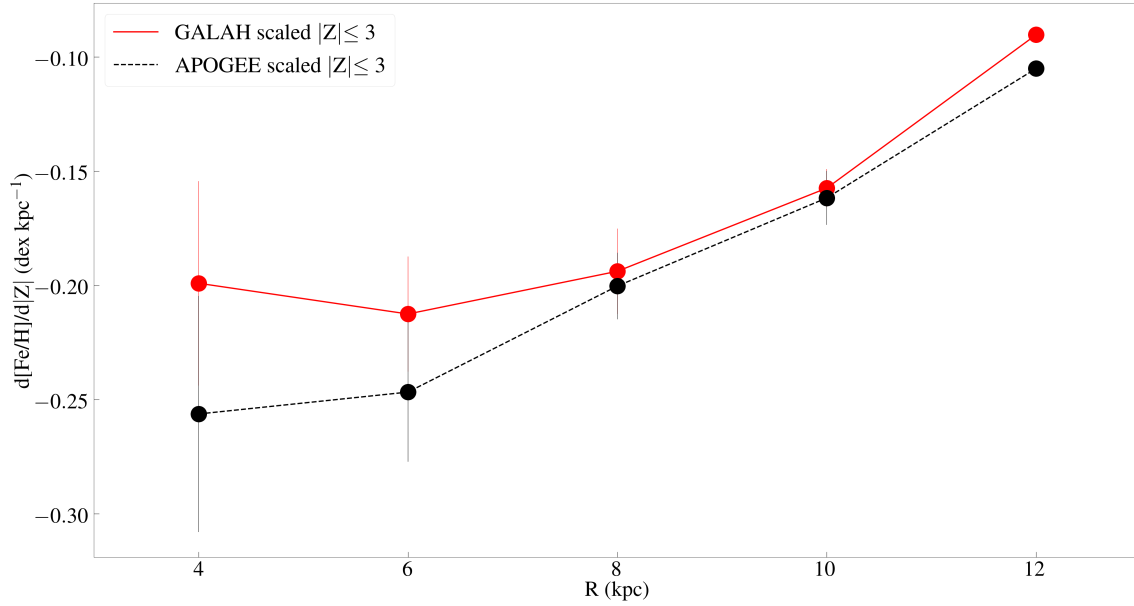


Figure 19. Vertical metallicity gradient, $d[Fe/H]/d|Z|$, vs Galactocentric distance, R , from 3 to 13 kpc for APOGEE scaled (black dashed line) and GALAH scaled (black line) samples showing the variation of vertical metallicity gradient from inner to outer regions. The black dots with the error bars represent the slopes of the gradients measured for stars in $|Z| \leq 3$ kpc within 2 kpc radial bins from 3 to 13 kpc. The slopes of the gradients within each R bin is measured by finding the median metallicity (black dots) in 0.3 kpc bins in $|Z|$ and then using a linear least-squares regression fit to the median metallicity at each $|Z|$ bin and the error bar is from the line fit to the median values. The negative vertical metallicity gradients seen using both the samples gradually becomes flatter as we move outwards from the inner regions.

Using a LAMOST anticentre sample (LSS-GAC; Huang et al. (2015)) measured vertical metallicity gradient of -0.146 ± 0.012 dex kpc^{-1} and -0.149 ± 0.012 dex kpc^{-1} for the sample in $7 \leq R \leq 8$ kpc and $8 \leq R \leq 9$ kpc, respectively. This is shallower than our estimates from both the samples. With main sequence turn-off stars in LSS-GAC, Xiang et al. (2015) measured a vertical metallicity gradient that is in the range of ~ -0.2 to -0.3 dex kpc^{-1} in the R bin of 8 to 9 kpc and $|Z| < 2$ kpc, that agrees well with our estimates. Schlesinger et al. (2014) carried out a detailed study of the vertical metallicity gradient using over 40,000 G-dwarf stars from the SEGUE DR9 catalogue range of 6.7 to 9.5 kpc in R and 0.27 to 1.62 kpc in $|Z|$, and estimated the gradient to be $-0.243^{+0.039}_{-0.053}$ dex kpc^{-1} . In an attempt to investigate the selection function effect in large scale surveys, Nandakumar et al. (2017) combined the common fields in APOGEE, LAMOST, RAVE and APOGEE, GES, RAVE, and estimated a mean vertical metallicity gradient of -0.241 ± 0.028 dex kpc^{-1} in the solar neighborhood, again slightly steeper owing to the $|Z| \leq 2$ kpc limit in their sample. Our solar neighborhood vertical gradient estimate is consistent with that estimated by Duong et al. (2018) (-0.22 ± 0.01 dex kpc^{-1}) using GALAH pilot survey sample within $7.9 \leq R \leq 9.5$ kpc, $|Z| < 2$ kpc. Ciucă et al. (2018) carried out a vertical metallicity gradient study using a sample of 18,435 dwarf stars within 500 pc of the Sun in R , $|Z|$ selected from the cross-matched Tycho-Gaia Astrometric Solution (TGAS) and RAVE Data Release 5. After taking into account the selection function effect, they estimated a flatter gradient ($-0.026^{+0.020}_{-0.021}$ dex kpc^{-1}) compared to our estimate (-0.31 ± 0.01 dex kpc^{-1} for APOGEE scaled sample and -0.23 ± 0.01 dex kpc^{-1} for GALAH scaled sample) within the same R , $|Z|$

range. This significant difference could be due to our large sample size (more than 10 times their sample size) and the evident low number statistics in the higher $|Z|$ regions in their sample where we find more metal poor stars in our sample driving the gradient down to negative values. They also divide their sample into five mono-age stellar populations between 0 and 11 Gyr, finding flat and steep vertical metallicity gradients for the youngest and oldest stellar populations respectively. They attribute this to the scenario where the mono age populations form from an initial flaring star-forming disc that has a negative radial metallicity gradient and undergoes radial mixing process (Kawata et al. 2017). Estimating reliable ages for our two survey scaled samples will enable us to investigate such mono age trends in metallicity gradients and compare with similar studies (e.g. Xiang et al. 2015; Anders et al. 2017; Ciucă et al. 2018 etc.).

5 SUMMARY AND CONCLUSIONS

We used the data driven approach, the *Cannon*, to put the stellar parameters and $[Fe/H]$ values from the latest data releases of two complementary high resolution spectroscopic surveys, APOGEE and GALAH, on the same scale. We chose training sets from among $\sim 20,000$ stars commonly observed in both the surveys. We trained high quality APOGEE spectra with high fidelity GALAH stellar labels and high quality GALAH spectra with high fidelity APOGEE stellar labels, chosen from the training sets. After cross validation, that pointed us to the limitations in the respective *Cannon* models, we derived

stellar parameters and $[\alpha/\text{Fe}]$ values from the APOGEE and GALAH spectra. After quality cuts based on the systematic trends between the two surveys seen in the training sets, SNR cuts, spectral flags as well as *Cannon* chi-square cuts, we end up with GALAH scaled stellar parameter catalogue for 486,690 stars/spectra and APOGEE scaled stellar parameter catalogue for 503,081 stars/spectra. A quick cross match between the two catalogues after parallax (*Gaia* DR2) cuts resulted in 436,470 stars/spectra with distances estimated by Bailer-Jones et al. (2018) that was used for further comparison study of Milky Way disc trends at different R and $|z|$ locations across the Galaxy.

We found APOGEE scaled sample to have mean metallicities that are higher compared to that for the GALAH scaled sample with the magnitude of difference varying according to the location in the Galaxy. Both the samples follow similar MDF trends : distributions shift toward metal poor values while moving away from the Galactic mid plane, while the mean metallicities/peaks of distributions at all heights (except $1 \leq |z| \leq 2$ kpc) tend to increase from the inner regions till the solar neighborhood and starts decreasing from there on to the outer regions. The skewness of the distributions change from negative to positive from inner to outer regions indicating the effect of radial mixing. The $[\alpha/\text{Fe}]$ distributions of both APOGEE and GALAH scaled samples show bi modality, while APOGEE scaled sample distribution is narrower with low α sequence concentrated close to the solar $[\alpha/\text{Fe}]$ value and high α sequence peaking at lower value than in the case of GALAH scaled sample.

We found the combined effect of the $[\text{Fe}/\text{H}]$ and $[\alpha/\text{Fe}]$ differences between the APOGEE and GALAH scaled samples getting reflected in the $[\alpha/\text{Fe}]$ vs $[\text{Fe}/\text{H}]$ trends. The resulting trends are consistent with the trends as seen with previous data releases of APOGEE, but with more number statistics in the APOGEE-GALAH survey R, $|z|$ overlap regions. The variation of the radial metallicity gradient with height from the plane and vertical metallicity gradient from inner to outer regions using APOGEE and GALAH scaled samples are consistent within the broad range found in the previous studies. This is especially true for the gradient estimates in the solar neighborhood close to the Galactic mid plane where most of the previous studies are concentrated. We estimate radial gradient of -0.03 ± 0.01 dex kpc^{-1} (GALAH scaled sample) and -0.04 ± 0.01 dex kpc^{-1} (APOGEE scaled sample) in the $7 \leq R \leq 9$ kpc, $|z| \leq 0.5$ kpc bin consistent with various studies in the literature using APOGEE, LAMOST, GES and RAVE surveys. Similarly, our vertical gradient estimate of -0.19 ± 0.02 dex kpc^{-1} (GALAH scaled sample) and -0.20 ± 0.02 dex kpc^{-1} (APOGEE scaled sample) in the same R, $|z|$ bin is consistent with the study using previous GALAH release as well as other surveys. Meanwhile, the differences between the gradients estimated by the two samples are more prominent in regions farther from the solar neighborhood.

Thus in this study we attempted to combine two complementary high resolution spectroscopic surveys, APOGEE and GALAH, by using the *Cannon* to scale one survey stellar parameters in terms of the other. We have made two catalogues of APOGEE scaled and GALAH scaled fundamental stellar parameters and general $[\alpha/\text{Fe}]$ abundances, and showed the differences in the Milky Way disc trends at different R and $|z|$ locations across the Galaxy using selected stars in them. We haven't carried out any selection function effect correction to this data, since for that we need age information in addition to metallicities and respective survey selection criteria. Accurate age estimates can also be used to carry out gradient studies for mono age populations. Thus all these are works for the future along with the inclusion of low resolution surveys (e.g. LAMOST) that will significantly increase the sample size and sky coverage.

ACKNOWLEDGEMENTS

Based on data acquired through the Australian Astronomical Observatory, under programmes: A/2013B/13 (The GALAH pilot survey); A/2014A/25, A/2015A/19, A2017A/18 (The GALAH survey phase 1), A2018 A/18 (Open clusters with HERMES), A2019A/1 (Hierarchical star formation in Ori OB1), A2019A/15 (The GALAH survey phase 2), A/2015B/19, A/2016A/22, A/2016B/10, A/2017B/16, A/2018B/15 (The HERMES-TESS program), and A/2015A/3, A/2015B/1, A/2015B/19, A/2016A/22, A/2016B/12, A/2017A/14, (The HERMES K2-follow-up program). We acknowledge the traditional owners of the land on which the AAT stands, the Gamilaraay people, and pay our respects to elders past and present.

LC is the recipient of the ARC Future Fellowship FT160100402.

Funding for the Sloan Digital Sky Survey IV has been provided by the Alfred P. Sloan Foundation, the U.S. Department of Energy Office of Science, and the Participating Institutions. SDSS acknowledges support and resources from the Center for High-Performance Computing at the University of Utah. The SDSS web site is www.sdss.org.

This work has made use of data from the European Space Agency (ESA) mission *Gaia* (<http://www.cosmos.esa.int/gaia>), processed by the *Gaia* Data Processing and Analysis Consortium (DPAC, <http://www.cosmos.esa.int/web/gaia/dpac/consortium>). Funding for the DPAC has been provided by national institutions, in particular the institutions participating in the *Gaia* Multilateral Agreement.

This publication made use of NASA's Astrophysics Data System.

DATA AVAILABILITY

The data underlying this article are available in the Data Central at https://cloud.datacentral.org.au/teamdata/GALAH/public/GALAH_DR3/

REFERENCES

- Abadi M. G., Navarro J. F., Steinmetz M., Eke V. R., 2003, *ApJ*, **597**, 21
 Adibekyan V. Z., Sousa S. G., Santos N. C., Delgado Mena E., González Hernández J. I., Israelian G., Mayor M., Khachatryan G., 2012, *A&A*, **545**, A32
 Ahumada R., et al., 2019, arXiv e-prints, p. arXiv:1912.02905
 Amarsi A. M., et al., 2020, *A&A*, **642**, A62
 Anders F., et al., 2014, *A&A*, **564**, A115
 Anders F., et al., 2017, *A&A*, **600**, A70
 Bailer-Jones C. A. L., Rybizki J., Foesneau M., Mantelet G., Andrae R., 2018, *AJ*, **156**, 58
 Barden S. C., et al., 2010, in Ground-based and Airborne Instrumentation for Astronomy III. p. 773509, doi:10.1117/12.856103
 Bedell M., et al., 2018, *ApJ*, **865**, 68
 Belokurov V., Erkal D., Evans N. W., Koposov S. E., Deason A. J., 2018, *MNRAS*, **478**, 611
 Bensby T., Feltzing S., Lundström I., 2003, *A&A*, **410**, 527
 Bergemann M., et al., 2014, *A&A*, **565**, A89
 Bird J. C., Kazantzidis S., Weinberg D. H., 2012, *MNRAS*, **420**, 913
 Blanton M. R., et al., 2017, *AJ*, **154**, 28
 Boeche C., et al., 2013, *A&A*, **559**, A59
 Boeche C., et al., 2014, *A&A*, **568**, A71
 Bournaud F., Elmegreen B. G., Martig M., 2009, *ApJ*, **707**, L1
 Bowen I. S., Vaughan A. H. J., 1973, *Appl. Opt.*, **12**, 1430
 Brook C. B., Kawata D., Gibson B. K., Freeman K. C., 2004, *ApJ*, **612**, 894
 Brook C. B., Gibson B. K., Martel H., Kawata D., 2005, *ApJ*, **630**, 298
 Brunetti M., Chiappini C., Pfenninger D., 2011, *A&A*, **534**, A75
 Buck T., 2020, *MNRAS*, **491**, 5435
 Buder S., et al., 2018, *MNRAS*, **478**, 4513
 Buder S., et al., 2019, *A&A*, **624**, A19

- Carrera R., et al., 2019, *A&A*, **623**, A80
- Casagrande L., Schönrich R., Asplund M., Cassisi S., Ramírez I., Meléndez J., Bensby T., Feltzing S., 2011, *A&A*, **530**, A138
- Casey A. R., Hogg D. W., Ness M., Rix H.-W., Ho A. Q. Y., Gilmore G., 2016, arXiv e-prints, p. arXiv:1603.03040
- Casey A. R., et al., 2017, *ApJ*, **840**, 59
- Chen L., Hou J. L., Wang J. J., 2003, *AJ*, **125**, 1397
- Ciucă I., Kawata D., Lin J., Casagrande L., Seabroke G., Cropper M., 2018, *MNRAS*, **475**, 1203
- Cui X.-Q., et al., 2012, *Research in Astronomy and Astrophysics*, **12**, 1197
- Cunha K., et al., 2016, *Astronomische Nachrichten*, **337**, 922
- Dalton G., et al., 2018, in *Ground-based and Airborne Instrumentation for Astronomy VII*. p. 107021B, doi:10.1117/12.2312031
- De Silva G. M., et al., 2015, *MNRAS*, **449**, 2604
- Duong L., et al., 2018, *MNRAS*, **476**, 5216
- Eisenstein D. J., et al., 2011, *AJ*, **142**, 72
- Fabbro S., Venn K. A., O'Briain T., Bialek S., Kielty C. L., Jahandar F., Monty S., 2018, *MNRAS*, **475**, 2978
- Freeman K., Bland-Hawthorn J., 2002, *ARA&A*, **40**, 487
- Fuhrmann K., 1998, *A&A*, **338**, 161
- Gaia Collaboration et al., 2016, *A&A*, **595**, A1
- Gaia Collaboration et al., 2018, *A&A*, **616**, A1
- García Pérez A. E., et al., 2016, *AJ*, **151**, 144
- Genovali K., et al., 2014, *A&A*, **566**, A37
- Gilmore G., Reid N., 1983, *MNRAS*, **202**, 1025
- Gilmore G., et al., 2012, *The Messenger*, **147**, 25
- Gunn J. E., et al., 2006, *AJ*, **131**, 2332
- Gustafsson B., Edvardsson B., Eriksson K., Jørgensen U. G., Nordlund Å., Plez B., 2008, *A&A*, **486**, 951
- Hartkopf W. I., Yoss K. M., 1982, *AJ*, **87**, 1679
- Hasselquist S., et al., 2020, arXiv e-prints, p. arXiv:2008.03603
- Hayden M. R., et al., 2014, *AJ*, **147**, 116
- Hayden M. R., et al., 2015, *ApJ*, **808**, 132
- Haywood M., Di Matteo P., Lehnert M. D., Katz D., Gómez A., 2013, *A&A*, **560**, A109
- Helmi A., Babusiaux C., Koppelman H. H., Massari D., Veljanoski J., Brown A. G. A., 2018, *Nature*, **563**, 85
- Ho A. Y. Q., et al., 2017, *ApJ*, **836**, 5
- Huang Y., et al., 2015, *Research in Astronomy and Astrophysics*, **15**, 1240
- Ibata R. A., Malhan K., Martin N. F., 2019, *ApJ*, **872**, 152
- Jacobson H. R., et al., 2016, *A&A*, **591**, A37
- Jönsson H., et al., 2020, *AJ*, **160**, 120
- Kawata D., Grand R. J. J., Gibson B. K., Casagrande L., Hunt J. A. S., Brook C. B., 2017, *MNRAS*, **464**, 702
- Kollmeier J. A., et al., 2017, arXiv e-prints, p. arXiv:1711.03234
- Kordopatis G., et al., 2011, *A&A*, **535**, A107
- Leung H. W., Bovy J., 2019, *MNRAS*, **483**, 3255
- Lin J., et al., 2020, *MNRAS*, **491**, 2043
- Loebman S. R., Debattista V. P., Nidever D. L., Hayden M. R., Holtzman J. A., Clarke A. J., Roškar R., Valluri M., 2016, *ApJ*, **818**, L6
- Majewski S. R., et al., 2017, *AJ*, **154**, 94
- Mikolaitis Š., et al., 2014, *A&A*, **572**, A33
- Minchev I., Famaey B., 2010, *ApJ*, **722**, 112
- Minchev I., Chiappini C., Martig M., 2014, *A&A*, **572**, A92
- Minniti D., et al., 2010, *New Astron.*, **15**, 433
- Minniti J. H., et al., 2020, *A&A*, **640**, A92
- Myeong G. C., Vasiliev E., Iorio G., Evans N. W., Belokurov V., 2019, *MNRAS*, **488**, 1235
- Nandakumar G., Schultheis M., Hayden M., Rojas-Arriagada A., Kordopatis G., Haywood M., 2017, *A&A*, **606**, A97
- Ness M., et al., 2012, *ApJ*, **756**, 22
- Ness M., et al., 2013, *MNRAS*, **430**, 836
- Ness M., Hogg D. W., Rix H. W., Ho A. Y. Q., Zasowski G., 2015, *ApJ*, **808**, 16
- Ness M., Hogg D. W., Rix H. W., Martig M., Pinsonneault M. H., Ho A. Y. Q., 2016, *ApJ*, **823**, 114
- Nissen P. E., Christensen-Dalsgaard J., Mosumgaard J. R., Silva Aguirre V., Spitoni E., Verma K., 2020, *A&A*, **640**, A81
- Perryman M. A. C., et al., 1997, *A&A*, **500**, 501
- Piskunov N., Valenti J. A., 2017, *A&A*, **597**, A16
- Quillen A. C., Minchev I., Bland-Hawthorn J., Haywood M., 2009, *MNRAS*, **397**, 1599
- Quinn P. J., Hernquist L., Fullagar D. P., 1993, *ApJ*, **403**, 74
- Reddy B. E., Lambert D. L., Allende Prieto C., 2006, *MNRAS*, **367**, 1329
- Rojas-Arriagada A., et al., 2017, *A&A*, **601**, A140
- Rojas-Arriagada A., et al., 2020, arXiv e-prints, p. arXiv:2007.13967
- Schlesinger K. J., et al., 2014, *ApJ*, **791**, 112
- Schönrich R., Binney J., 2009, *MNRAS*, **399**, 1145
- Sellwood J. A., Binney J. J., 2002, *MNRAS*, **336**, 785
- Sharma S., et al., 2018, *MNRAS*, **473**, 2004
- Sharma S., et al., 2019, *MNRAS*, **490**, 5335
- Sharma S., Hayden M. R., Bland-Hawthorn J., 2020, arXiv e-prints, p. arXiv:2005.03646
- Sheinis A., et al., 2015, *Journal of Astronomical Telescopes, Instruments, and Systems*, **1**, 035002
- Skrutskie M. F., et al., 2006, *AJ*, **131**, 1163
- Steinmetz M., et al., 2006, *AJ*, **132**, 1645
- Stoughton C., et al., 2002, *AJ*, **123**, 485
- Taylor M. B., 2005, in *Shopbell P., Britton M., Ebert R., eds, Astronomical Society of the Pacific Conference Series Vol. 347, Astronomical Data Analysis Software and Systems XIV*. p. 29
- Taylor M. B., 2020, in *Ballester P., Ibsen J., Solar M., Shortridge K., eds, Astronomical Society of the Pacific Conference Series Vol. 522, Astronomical Data Analysis Software and Systems XXVII*. p. 67
- Ting Y.-S., Conroy C., Rix H.-W., Cargile P., 2019, *ApJ*, **879**, 69
- Valenti J. A., Piskunov N., 1996, *A&AS*, **118**, 595
- Vincenzo F., Kobayashi C., 2020, *MNRAS*, **496**, 80
- Weinberg D. H., et al., 2019, *ApJ*, **874**, 102
- Wheeler A., et al., 2020, *ApJ*, **898**, 58
- Wilson J. C., et al., 2019, *PASP*, **131**, 055001
- Wittenmyer R. A., et al., 2018, *AJ*, **155**, 84
- Wolf C., et al., 2018, *Publ. Astron. Soc. Australia*, **35**, e010
- Xiang M.-S., et al., 2015, *Research in Astronomy and Astrophysics*, **15**, 1209
- Xiang M., et al., 2019, *ApJS*, **245**, 34
- Yong D., Carney B. W., Teixeira de Almeida M. L., Pohl B. L., 2006, *AJ*, **131**, 2256
- Yoshii Y., 1982, *PASJ*, **34**, 365
- Zhang X., Zhao G., Yang C. Q., Wang Q. X., Zuo W. B., 2019, *PASP*, **131**, 094202
- de Jong R. S., et al., 2019, *The Messenger*, **175**, 3

This paper has been typeset from a $\text{\TeX}/\text{\LaTeX}$ file prepared by the author.